THESIS FOR THE DEGREE OF DOCTOR OF PHILOSOPHY

Generation and characterization of microwave quantum states

INGRID STRANDBERG

Department of Microtechnology and Nanoscience (MC2)
Applied Quantum Physics Laboratory
Chalmers University of Technology
Göteborg, Sweden, 2022

Generation and characterization of microwave quantum states
INGRID STRANDBERG
ISBN 978-91-7905-671-1

Doktorsavhandlingar vid Chalmers tekniska högskola
Ny serie nr 5137
ISSN 0346-718X

Applied Quantum Physics Laboratory
Department of Microtechnology and Nanoscience (MC2)
Chalmers University of Technology
SE–412 96 Göteborg
Sweden
Telephone +46 (0)31-772 1000

Cover: The author's artistic rendition of the generation and detection of microwave quantum states of light.

Chalmers Digitaltryck
Göteborg, Sweden, 2022

Generation and characterization of microwave quantum states
INGRID STRANDBERG
Applied Quantum Physics Laboratory
Department of Microtechnology and Nanoscience (MC2)
Chalmers University of Technology

Abstract

Quantum mechanics is the branch of physics that describes the properties and behavior of systems on the atomic and subatomic level. Over the past decades there has also been considerable progress in engineering larger-scale quantum systems. In this day and age, quantum information and quantum technology are rapidly developing areas of research where quantum effects are harnessed to improve sensitivity in measurements, encrypt secure communications, and enhance the performance of information processing and computing. Specific types of quantum states are needed for these purposes, and they can be challenging to generate in practice. This thesis describes methods to generate and characterize microwave states that could be useful for quantum computing protocols based on quantum states of light.

Keywords: Continuous-variable quantum computing, quantum states of light, quantum state engineering, superconducting quantum optics, quantum state tomography, multimode entanglement

Acknowledgments

My first thanks goes without a doubt to Fernando Quijandría, who was officially my co-supervisor but has in practice been my main source of supervision. I simply cannot overstate how important you have been for me and my development as a researcher; bringing me on to projects and discussing questions. I have very much enjoyed working with you and feel very lucky to have had you as my supervisor.

I also want to give a huge thanks to my main supervisor Göran Johansson for unceasingly providing a calm and positive presence, and for always being happy to talk—whether about work or just chit-chat.

Thanks to both present and former members of AQP for making this such an enjoyable workplace. You are not only good colleagues, but also good friends. Big thanks to Yong Lu and Marina Kudra for successful experimental collaborations, I'm very happy to have worked with you. Also shoutout to the other nice people at QT.

Non-work-related thanks goes to my weightlifting coach Martin Rothwall and training friends, my Engineering Physics gang, my bestie Christian von Schultz and my sister Helena Strandberg.

Finally, I want to thank myself for having confidence to never doubt that I could do this.

Ingrid Strandberg, Göteborg, August 2022

List of publications

This thesis is based on the following papers:

A Steady-state generation of Wigner negative states in 1D resonance fluorescence
Fernando Quijandría, **Ingrid Strandberg**, Göran Johansson
Phys. Rev. Lett. **121**, 263603 (2018)

B Numerical study of Wigner negativity in one-dimensional steady-state resonance fluorescence
Ingrid Strandberg, Yong Lu, Fernando Quijandría, Göran Johansson
Phys. Rev. A **100**, 063808 (2019)

C Propagating Wigner-negative states generated from the steady-state emission of a superconducting qubit
Yong Lu, **Ingrid Strandberg**, Fernando Quijandría, Göran Johansson, Simone Gasparinetti, Per Delsing
Phys. Rev. Lett. **126**, 253602 (2021)

D Wigner negativity in the steady-state output of a Kerr parametric oscillator
Ingrid Strandberg, Göran Johansson, Fernando Quijandría
Phys. Rev. Research **3**, 023041 (2021)

E Robust preparation of Wigner-negative states with optimized SNAP-displacement sequences
Marina Kudra, Mikael Kervinen, **Ingrid Strandberg**, Shahnawaz Ahmed, Marco Scigliuzzo, Amr Osman, Daniel Pérez Lozano, Giulia Ferrini, Jonas Bylander, Anton Frisk Kockum, Fernando Quijandría, Per Delsing, Simone Gasparinetti
PRX Quantum **3**, 030301 (2022)

F Multipartite entanglement in a microwave frequency comb
Shan W. Jolin, J. C. Rivera Hernández, David B. Haviland, Gustav Andersson, **Ingrid Strandberg**, Fernando Quijandría, Joe Aumentado, Riccardo Borgani, Mats O. Tholén
arXiv:2112.12105

G Simple, reliable and noise-resilient continuous-variable quantum state tomography with convex optimization
Ingrid Strandberg
arXiv:2202.11584

Other papers that are outside the scope of this thesis:

I Engineering symmetry-selective couplings of a superconducting artificial molecule to microwave waveguides
Mohammed Ali Aamir, Claudia Castillo Moreno, Simon Sundelin, Janka Biznárová, Marco Scigliuzzo, Kowshik Erappaji Patel, Amr Osman, D. P. Lozano, **Ingrid Strandberg**, Simone Gasparinetti
arXiv:2202.12209 (Accepted in PRL)

II PennyLane: Automatic differentiation of hybrid quantum-classical computations
V. Bergholm, J. Izaac, M. Schuld, C. Gogolin, S. Ahmed, V. Ajith, M. S. Alam, G. Alonso-Linaje, B. AkashNarayanan, A. Asadi, J. M. Arrazola, U. Azad, S. Banning, C. Blank, T. R. Bromley, B. A. Cordier, J. Ceroni, A. Delgado, O. Di Matteo, A. Dusko, T. Garg, D. Guala, A. Hayes, R. Hill, A. Ijaz, T. Isacsson, D. Ittah, S. Jahangiri, P. Jain, E. Jiang, A. Khandelwal, K. Kottmann, R. A. Lang, C. Lee, T. Loke, A. Lowe, K. McKiernan, J. J. Meyer, J. A. Montañez-Barrera, R. Moyard, Z. Niu, L. J. O'Riordan, S. Oud, A. Panigrahi, C-Y Park, D. Polatajko, N. Quesada, C. Roberts, N. Sá, I. Schoch, B. Shi, S. Shu, S. Sim, A. Singh, **I. Strandberg**, J. Soni, A. Száva, S. Thabet, R. A. Vargas-Hernández, T. Vincent, N. Vitucci, M. Weber, D. Wierichs, R. Wiersema, M. Willmann, V. Wong, S. Zhang, N. Killoran
arXiv:1811.04968v4

Contents

Chapter 1

Overview

The aim of this chapter is to provide background and context for the appended papers, which are to be described in the upcoming chapters. As the title of the thesis is "Generation and characterization of microwave quantum states", Chapter 2 is focused on quantum state *generation* and Chapter 3 centers on state *characterization*. Before that, this introductory chapter will provide an overview of essential concepts that form the foundation of this work: continuous-variable quantum computing, quantized microwave fields in superconducting circuits, and the phase space representation of quantum states. The reader is assumed to possess a basic knowledge of classical and quantum physics, but the goal is for this thesis to be comprehensible to a broad audience.

If you are not in the mood to read much more than one page, Chapter 4 aims to provide a concise summary of the contents of this thesis. Future prospects are also outlined at the end.

1.1 Introduction

When it comes to the smallest components of our universe, classical models of physics cease to apply. Since the advent of quantum mechanics in the 1920s we have improved our understanding about the quantum nature of the small-scale world. Knowledge of quantum physics has already been imperative for the development of electronic devices based on semiconductor components such as transistors, but now, the goal is to not only have devices whose hardware is described by quantum physics, but devices that actually process quantum information. Quantum information science is an interdisciplinary field connecting quantum mechanics and information theory. Since information is stored, transmitted and processed by physical means, the concept of information and computation can be formulated in the context of a physical theory such as quantum mechanics [1]. It has been demonstrated that technology utilizing characteris-

tically quantum phenomena can have advantages over classical counterparts in fields such as metrology[1] and sensing [2], communication and cryptography [3], and computing [4]. Research in quantum computing is now attracting considerable amounts of attention from both academic researchers and industry[2] worldwide. The great interest stems from the fact that a quantum computer running quantum algorithms can in theory solve certain computational problems faster than a classical computer, and perform computations that are intractable for even the most powerful supercomputers. This is called *quantum advantage*. However, not all quantum states can provide this advantage. The work presented in this thesis is focused on the generation and characterization of states that could be resources for quantum computing. In particular, we focus on quantum states of the electromagnetic field.

1.2 Continuous-variable quantum computing with microwaves

There are different approaches to quantum computing. The perhaps most well-known example is computing with quantum bits—qubits. Analogously to ordinary bits, qubits are described as two-level systems which have two discrete energy levels we can label as 0 and 1. But there exists an alternative to discrete variable quantum computing: *continuous-variable* (CV) quantum computing [5, 6]. In the CV approach we utilize observables characterized by a continuous spectrum, such as the quadratures of an electromagnetic field[3] which will be defined later.

The electromagnetic spectrum contains light with a wide range of frequencies, as illustrated in Fig. 1.1. While the theory in this thesis applies to any wavelength, the experiments in Papers C, E and F were performed in the microwave frequency range with superconducting circuits. The discipline of superconducting circuits interacting with quantized microwave fields is called circuit quantum electrodynamics (circuit-QED). This is a prominent platform for quantum computing, and we will get back to this subject in Section 1.5. Before that, I introduce quantization of the electromagnetic field and the concept of modes.

1.3 The quantized electromagnetic field

In the year 1865 James Clerk Maxwell published a paper [7] where he concluded that light is an electromagnetic wave. The classical theory of light is given by

[1] Metrology is the study of measurement, not to be confused with *meteorology* which is the study of weather.

[2] Just to name a few, companies such as Google, IBM, Microsoft and Amazon are making large investments in research and development of a quantum computer.

[3] Other approaches to CV are to use motional states of a nanomechanical oscillator or trapped ions.

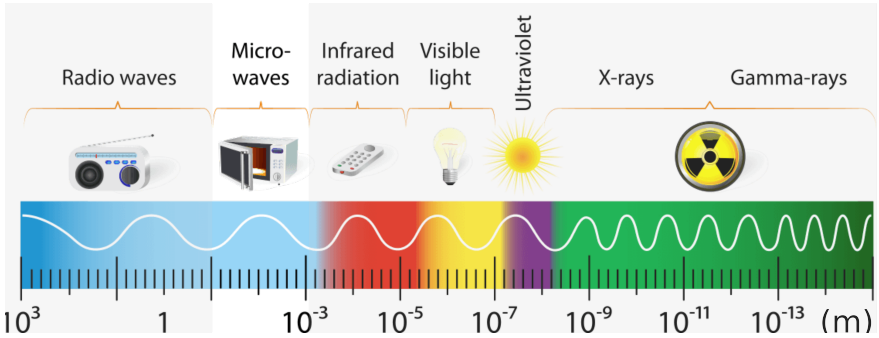

Figure 1.1: The electromagnetic spectrum. The microwave regime is highlighted, and the wavelength in meters is indicated at the bottom.

Maxwell's equations, which in the Coulomb gauge give the wave equation

$$\left(\nabla^2 - \frac{1}{c^2}\frac{\partial^2}{\partial t^2}\right)\vec{E}(\vec{r},t) = 0, \tag{1.1}$$

for the classical electric vector field $\vec{E}$ in the absence of charges and currents. A solution to this equation that also satisfies the appropriate boundary conditions is called a *mode*. A general solution to the wave equation can be expressed as a linear combination [8]

$$\vec{E}(\vec{r},t) = \sum_n \tilde{\alpha}_n \vec{f}_n(\vec{r},t) + \tilde{\alpha}_n^* \vec{f}_n^*(\vec{r},t), \tag{1.2}$$

where $\tilde{\alpha}_n$ are complex mode coefficients and each f_n is a *spatio-temporal* mode function that satisfies the wave equation under the applied boundary conditions. Generally the boundary conditions allow only a discrete set of solutions. A field that has more than one nonzero term in the sum is a multimode field where the index n labels the different frequency modes. Note that this discreteness has nothing to do with quantization, it solely arises from the spatial boundary condition. Assuming periodic boundary conditions, the solution can be written as an expansion in running plane waves [9–11]

$$\vec{E}(\vec{r},t) = \sum_n \sqrt{\frac{\hbar\omega_n}{2V\varepsilon_0}}\left(\alpha_n e^{\mathrm{i}(\vec{k}_n\cdot\vec{r}-\omega_n t)} + \alpha_n^* e^{-\mathrm{i}(\vec{k}_n\cdot\vec{r}-\omega_n t)}\right), \tag{1.3}$$

where the mode coefficients have been scaled as $\tilde{\alpha}_n = \sqrt{\hbar\omega_n/2V\varepsilon_0}\alpha_n$ such that α_n is dimensionless. The field is presumed to occupy an empty volume V, ε_0 is the vacuum permittivity[4], and $\hbar$ is the reduced Planck constant which we conventionally set to 1 from now on. The frequency ω_n is related to the wave

[4]These constants are not important for the point of this chapter, but are included for correctness.

vector $\vec{k}_n$ via the linear dispersion relation $|\vec{k}_n| = \omega_n/c$ with c being the speed of light.

Light can indeed behave as a wave, but it can also be observed to have a particle-like nature. This is called the particle-wave duality in quantum theory, which became a necessity to describe some physical phenomena. For example, in the year 1900 Max Planck observed that the energy of thermal radiation could be correctly calculated if one assumed that electromagnetic radiation could be emitted or absorbed only in discrete packets [12]. These packets called "quanta" are now known as photons. When the field is quantized[5], the mode coefficient α_n is promoted to an operator $\hat{a}_n$ called the photon-annihilation operator and its complex conjugate α_n^* becomes the photon-creation operator $\hat{a}_n^\dagger$. These operators obey the bosonic commutation relation

$$[\hat{a}_{n'}, \hat{a}_n^\dagger] = \delta_{n'n}. \tag{1.4}$$

For a single mode of frequency ω, this is the commutation relation $[\hat{a}, \hat{a}^\dagger] = 1$ of the ladder operators describing a quantum harmonic oscillator with Hamiltonian $H = \omega\hat{a}^\dagger\hat{a}$. Indeed, a single-mode electromagnetic field is modelled as a simple harmonic oscillator. Since most of the work in this thesis is on single-mode fields, we will consider this case in the rest of the introduction, denoting the field operators simply by $\hat{a}$, $\hat{a}^\dagger$, which removes and adds a photon to the mode, respectively.

Quadrature operators

The number of photons is a discrete observable, but as previously mentioned, the quantum state of an electromagnetic field also has observables with a continuous spectrum: the *quadratures*. The $\hat{x}$ and $\hat{p}$ quadratures are conjugate variables, defined as

$$\begin{aligned} \hat{x} &= \frac{1}{\sqrt{2}}(\hat{a}^\dagger + \hat{a}), \\ \hat{p} &= \frac{\mathrm{i}}{\sqrt{2}}(\hat{a}^\dagger - \hat{a}). \end{aligned} \tag{1.5}$$

The quantized version of Eq. (1.3) for a single mode is

$$\hat{E}(\vec{r}, t) = \mathcal{E}_0(\hat{a}e^{\mathrm{i}(\vec{k}\cdot\vec{r}-\omega t)} + \hat{a}^\dagger e^{-\mathrm{i}(\vec{k}\cdot\vec{r}-\omega t)}), \tag{1.6}$$

where $\mathcal{E}_0$ contains the dimensional prefactors. Inserting Eqs. (1.5) into this gives

$$\hat{E}(\vec{r}, t) = \sqrt{2}\mathcal{E}_0 \left(\hat{x}\cos(\vec{k}_n \cdot \vec{r} - \omega_n t) + \hat{p}\sin(\vec{k}_n \cdot \vec{r} - \omega_n t)\right), \tag{1.7}$$

which provides an intuitive interpretation of the quadratures as the sine and cosine parts of the field (illustrated in Fig. 1.2). As the notation implies, the

[5] Traditionally the variables are given hats to indicate that they are no longer c-numbers but operators.

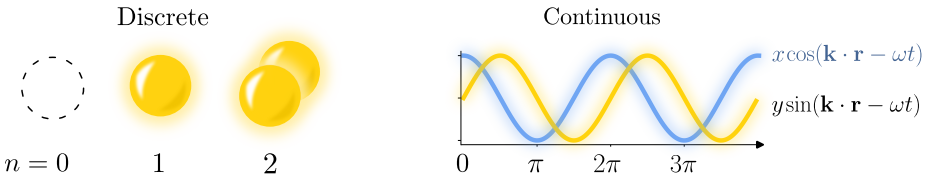

Figure 1.2: A quantum state of light has both discrete and continuous degrees of freedom. The radiation field can be decomposed into one component in phase with a reference $\cos(\vec{k}\cdot\vec{r}-\omega t)$ and one out of phase with it.

quadratures are in a certain sense also analogous to position and momentum, since they obey the same canonical commutation relation

$$[\hat{x},\hat{p}] = \mathrm{i}. \tag{1.8}$$

And just as position x and momentum p are ordinarily coordinates in phase space, eigenvalues of the quadrature operators $\hat{x}$, $\hat{p}$ are also phase space coordinates.

Phase space representation: Wigner function

A quantum state is commonly described by a density operator ρ acting on the Hilbert space of the system in question. But a CV state can also be described by a function in phase space. The Heisenberg uncertainty principle forbids the definition of a joint probability distribution at a point (x,p) in phase space since the corresponding operators do not commute, but it is possible to define *quasiprobability* distributions [13]. Quasiprobability distributions are called such because unlike proper probability distributions they are not required to be strictly positive. There exist many quantum phase space distributions, but commonly used is the *Wigner function*. It is defined in terms of the density matrix ρ as [14]

$$W(x,p) = \frac{1}{2\pi}\int_{-\infty}^{\infty} \mathrm{d}y\, e^{-\mathrm{i}py}\, \langle x+\frac{y}{2}|\rho|x-\frac{y}{2}\rangle\,, \tag{1.9}$$

where x and p are the previously mentioned quadratures. Among all quantum phase space distributions, the Wigner function is special and useful in several ways: it is always real-valued, and integrating it along a direction in phase space gives a genuine probability distribution of the orthogonal quadrature. For example, integrating over p gives a probability distribution in x. It can also be directly measured experimentally [15–17]. Negativity of the Wigner function is a signature of nonclassicality, and importantly for the field of quantum computing, Wigner-negativity has been shown to be a necessity for the possibility of a

quantum advantage[6] [18–21]. As an example, a contour plot of the Wigner function for a single-photon is shown in Fig. 1.3.

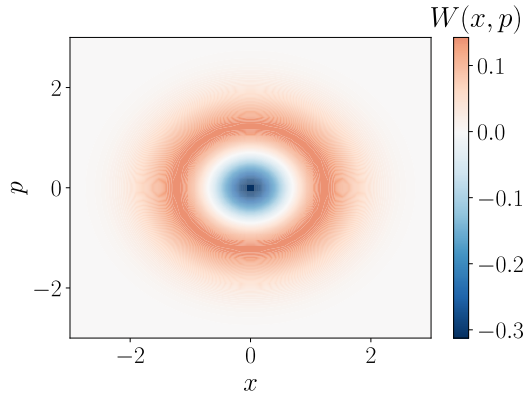

Figure 1.3: Wigner function of the single photon state $\rho = |1\rangle\langle 1|$. The region in the middle takes negative values, indicating nonclassicality of the state.

1.4 Universal quantum computing

A universal computer can perform any computation. For a quantum computer this corresponds to the ability to perform any arbitrary unitary operation on its states [22]. A quantum algorithm or computation is commonly represented as a circuit. A sketch of a generic circuit is displayed in Fig. 1.4. It is composed of three parts: input states, the unitary operations, and measurements which provide the final output. For a quantum computer to be universal, at least one of these three parts have to be *non-Gaussian*[7]. A Gaussian state has by definition a Gaussian Wigner function, which is positive. The Wigner function of a quantum state was introduced in Eq. (1.9), and any operation during the steps of a quantum computation can also be represented as a state via the Choi-Jamiolkowski correspondence [25, 26].

The Gaussian shape of the vacuum Wigner function is shown in the surface plot in Fig. 1.5 as an example. For pure states there is a one-to-one relation between non-Gaussianity and Wigner negativity [27]. While the situation is less clear-cut for mixed states, a state that is Wigner-negative is necessarily non-Gaussian. Gaussian unitary operations and states are generated by Hamiltonians that are at most quadratic in the field operators $\hat{a}$, $\hat{a}^\dagger$ (or equivalently $\hat{x}$

[6] Technically, it was shown that quantum computations represented by positive Wigner functions can be efficiently simulated on a classical computer, but clearly any quantum circuit that can be efficiently simulated classically offers no quantum advantage.

[7] Correspondingly for a qubit-based computer, so-called *magic states* [23] or *non-Clifford* operations [24] are needed for universality.

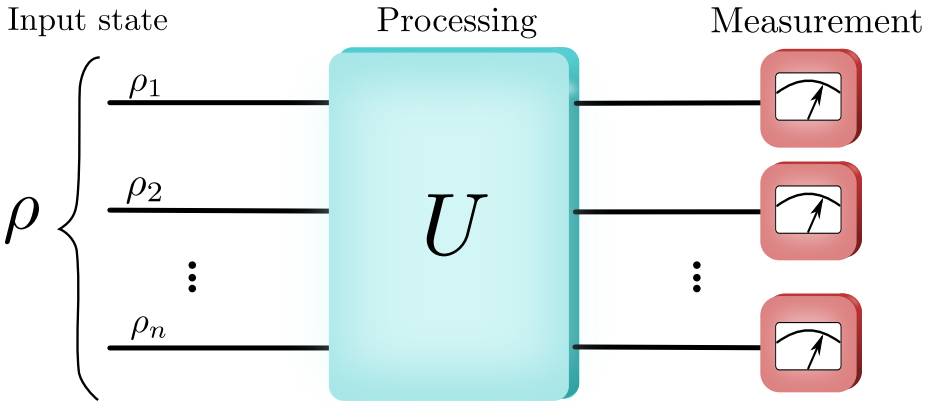

Figure 1.4: A quantum circuit with multiple modes or qubits represented by the horizontal lines, with the input state to the left. Unitary operations are performed on the system, and local measurements at the end.

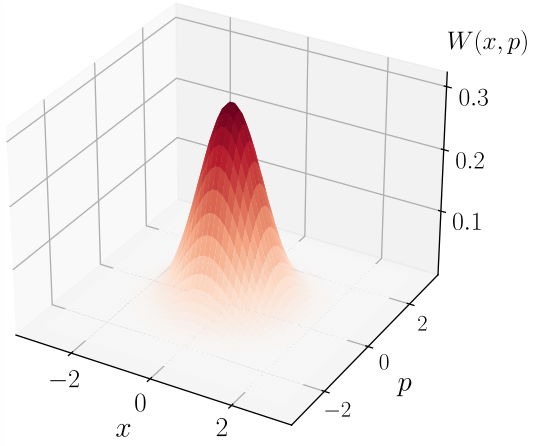

Figure 1.5: The Gaussian Wigner function of the vacuum state $\rho = |0\rangle\langle 0|$. Inserting this in Eq. (1.9), it can be analytically calculated to $W(x,p) = e^{-(x^2+p^2)}/\pi$.

and $\hat{p}$). The time-evolution of such a Hamiltonian corresponds to linear transformations of the field operators. Hence, in order to simulate Hamiltonians of any arbitrary polynomial order of field operators, a universal quantum computer must include a cubic or higher order nonlinearity to obtain universality and Wigner-negativity.

1.5 Superconducting circuits

The circuit-QED platform is useful for quantum computing since the Josephson junction provides a versatile nonlinearity. It is the principal component in superconducting qubits [28], and consists of two superconducting electrodes separated by a thin insulating barrier and can be described as a nonlinear inductance[8] L_J [29]

$$L_\mathrm{J} = \frac{\Phi_0}{2\pi I_c \cos\varphi}, \tag{1.10}$$

which depends on the phase difference $\varphi = \varphi_1 - \varphi_2$ across the junction [as illustrated in Fig. 1.6(a)], and the critical current[9] I_c. The constant Φ_0 is the magnetic flux quantum.

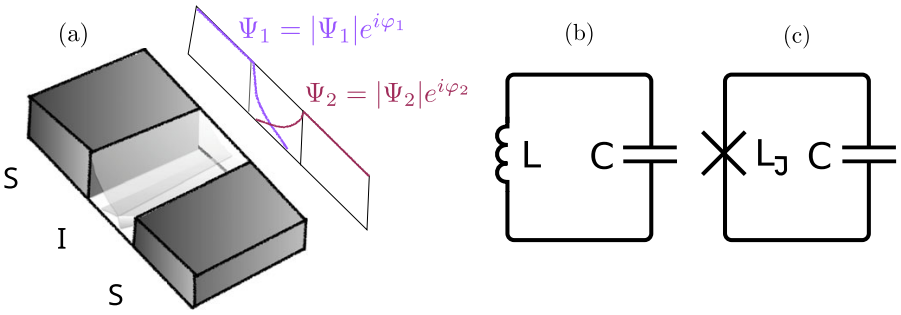

Figure 1.6: (a) Schematic illustration of a Josephson junction, which consists of an insulator I sandwiched between two superconductors S to make a SIS tunnel junction. A supercurrent of Cooper pairs can tunnel through the junction if the wave functions Ψ_1 and Ψ_2 of the superconducting condensates overlap in the barrier [30]. (b) Circuit diagram of a linear LC-circuit. (c) Nonlinear resonator where the linear inductance L is replaced by a Josephson junction represented as a lumped circuit element with nonlinear inductance L_J.

Consider first a linear electrical circuit like Fig. 1.6(b). Methods of analytical mechanics can be applied to electrical circuits [31], and this is done prior to quantization as conjugate variables are naturally defined as generalized coordinates. The Hamiltonian of a plain LC-oscillator with characteristic frequency $\omega_0 = 1/\sqrt{LC}$ is

$$H_{LC} = \frac{Q^2}{2C} + \frac{\Phi^2}{2L}, \tag{1.11}$$

[8] A real junction also has resistive properties because of Cooper pairs being broken up by thermal excitations, and it also has a capacitance due to essentially being a parallel-plate capacitor. But it can be operated in a regime where these effects are not detrimental for our purpose of utilizing the nonlinear inductance.

[9] The critical current is the maximal supercurrent a superconductor can carry.

where Q is the charge on the capacitor and Φ is the magnetic flux through the inductor. These conjugate variables are then quantized by imposing the canonical commutation relation

$$[\hat{\Phi}, \hat{Q}] = \mathrm{i}. \tag{1.12}$$

As an LC-circuit is an electric harmonic oscillator, it useful to introduce the standard annihilation $\hat{a}$ and creation $\hat{a}^\dagger$ operators of the harmonic oscillator such that

$$\hat{\Phi} = \sqrt{\frac{Z}{2}}\left(\hat{a}^\dagger + \hat{a}\right), \quad \hat{Q} = \mathrm{i}\sqrt{\frac{1}{2Z}}\left(\hat{a}^\dagger - \hat{a}\right), \tag{1.13}$$

where $Z = \sqrt{L/C}$ is the characteristic impedance of the circuit. Now if the linear inductance L is replaced by a Josephson junction, a term

$$\hat{H}_\mathrm{J} = E_\mathrm{J} \cos\left(\frac{2\pi}{\Phi_0}\hat{\Phi}\right) \tag{1.14}$$

is added to the Hamiltonian, where the relation between the phase difference φ in Eq. (1.10) and the flux is $\varphi = 2\pi\Phi/\Phi_0$. The constant $E_\mathrm{J} = \Phi_0 I_c/2\pi$ is called the Josephson energy [32, 33]. Taylor expanding the cosine, one can see second- and higher-order terms of $\hat{\Phi}$ (or equivalently $\hat{a}$ and $\hat{a}^\dagger$) are obtained, meaning that the circuit essentially is a nonlinear oscillator. The form of a superconducting circuit Hamiltonian can be engineered by designing different circuits with Josephson junctions [34, 35].

1.5.1 SQUID

Two Josephson junctions with equal inductance $L_\mathrm{J}/2$ can be placed in parallel in a superconducting loop to form a so-called superconducting quantum interference device (SQUID)[10]. This is a useful device that can be used for very sensitive measurements of weak magnetic fields [36, 37], but we will use it as a tunable inductance. It has an inductance $L_\mathrm{J}^\mathrm{SQUID}$

$$L_\mathrm{J}^\mathrm{SQUID} = \frac{L_\mathrm{J}}{\cos\left|\pi\Phi_\mathrm{ext}/\Phi_0\right|}, \tag{1.15}$$

that is dependent on an external magnetic flux Φ_ext through the SQUID loop. The device is illustrated in Fig. 1.7.

The flux can be modulated[11] to induce so-called *parametric* effects. The word "parametric" is used for energy-conserving processes in which a nonlinear medium is used for mixing different frequencies by modulating some parameter of the system in time [39]. In a circuit-QED setup, the time-varying parameter is often the SQUID inductance. Parametric effects will be used to drive the system in Section 2.2.2 and create entanglement in Section 3.1.

[10] More specifically, this is called a dc SQUID.

[11] An alternative is to modulate the current, but we will use a flux pump.

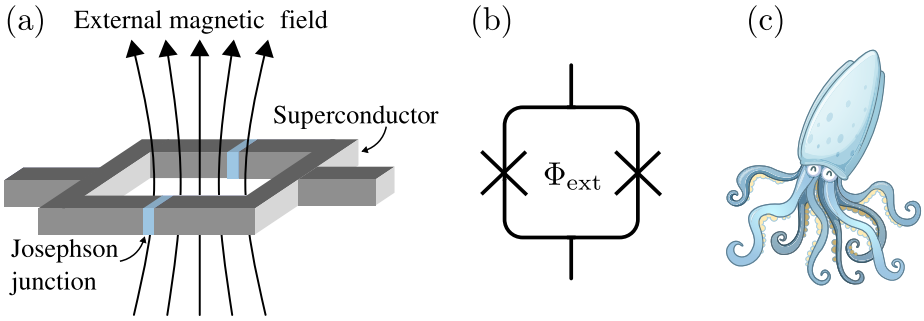

Figure 1.7: Superconducting quantum interference device (SQUID). (a) Schematic of implementation. (b) Circuit diagram. (c) Wrong type of squid. Figs. (a), (b) adapted from [38], (c) from Vecteezy.com.

1.5.2 Linear microwave components

A nonlinear circuit component is often coupled to a microwave field via a coplanar transmission line resonator [40], illustrated in Fig. 1.8(a). This is a type of planar waveguide that can confine the field to sub-wavelength size in the transverse dimension, meaning it is essentially a one-dimensional transmission line [41]. This is utilized for the propagating states in Section 2.2.

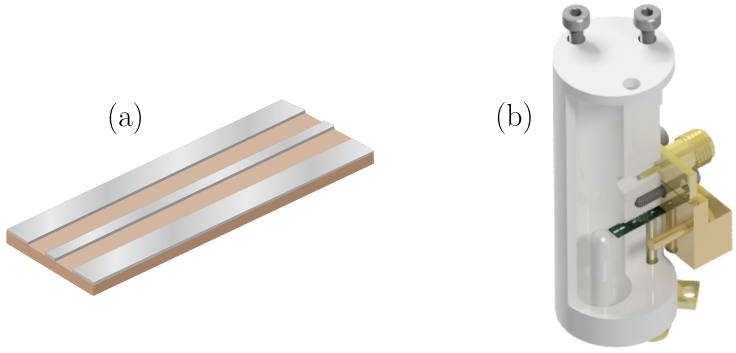

Figure 1.8: Two different linear microwave components that guide and confine the field, respectively. (a) Coplanar waveguide consisting of a center conductor and outer ground planes on a dielectric substrate. It is used to transmit microwave signals. (b) Three-dimensional cavity. This one is equipped with microwave antennas and a chip holder for a qubit and planar readout resonator. Credit to M. Kudra for Fig. (b).

Instead of transmitting a field, resonators can also be used to confine it. For this purpose, three-dimensional cavities are preferred since they can have orders

of magnitude larger quality factors[12] than planar resonators [42]. This type of resonator is shown in Fig. 1.8(b) and used in Section 2.3.

1.5.3 Quadrature measurements

There are several different schemes for measuring quantum states of light. A non-Gaussian type of measurement is photon-number resolving detection, which works by transforming the energy of an incoming photon into a measurable electrical signal. There are efficient detectors of this type for photons in the visible to near-infrared frequency range [43, 44], but there are currently no detectors that can reliably[13] resolve single microwave photons as they have four- to five orders of magnitude lower energy. We can instead measure the field quadratures. The simplest quadrature measurement is *homodyne* detection, which is commonly used in quantum optics. A typical textbook homodyne setup is shown in Fig. 1.9(a), and it measures the *generalized quadrature* [11]

$$\hat{x}_\theta = \frac{1}{\sqrt{2}}(\hat{a}^\dagger e^{\mathrm{i}\theta} + \hat{a}e^{-\mathrm{i}\theta}), \tag{1.16}$$

that is rotated relative to $\hat{x}$ in Eq. (1.5) by the angle θ as illustrated in Fig. 1.9(b). This angle is controlled by setting the phase of a local oscillator. Homodyne measurements will be simulated in Section 2.2.1.

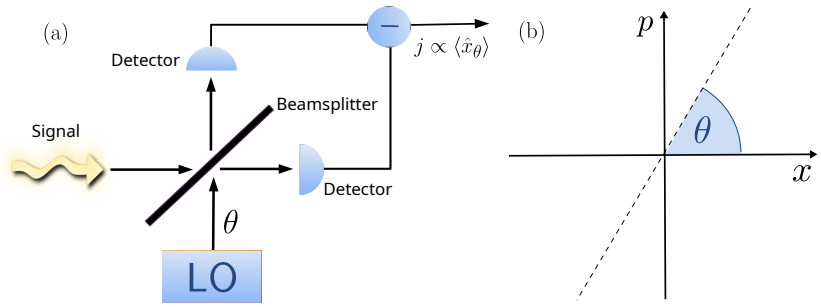

Figure 1.9: Schematic sketch of balanced homodyne detection. (a) The quantum signal is mixed with the signal of a local oscillator with reference phase θ on a 50:50 beamsplitter[14]. The amplitude of the two output fields are detected separately and subtracted, and the resulting signal j is proportional to the expectation value $\langle \hat{x}_\theta \rangle$. (b) Direction of the generalized quadrature x_θ in phase space.

[12] The quality factor describes the ability of a resonator to store energy, which in this case corresponds to the lifetime of a quantum state inside it.

[13] There exist microwave single-photon detectors, but they are complicated experiments by themselves and only have around 60 % detection efficiency [45, 46].

[14] IQ-mixers and low-pass filtering are used in the microwave regime instead of an optical beamsplitter [33].

Microwave homodyne detection is extra susceptible to electronic noise, so more common for microwave fields is *heterodyne* detection [32]. This is a slightly more involved procedure as it measures two quadratures simultaneously, and can be seen as "double homodyne" detection. It was used for the experiments described in Sections 2.2 and 3.1, and such measurement data is used to characterize states in Section 3.2. Both homo- and heterodyning are Gaussian measurements and are thus not resourceful for quantum computation by themselves. For this reason, we focus on state generation.

Chapter 2

Generation of Wigner-negative states

As mentioned in Chapter 1, Wigner negativity is an important property for quantum computing. It is a prerequisite for a quantum computer to obtain an exponential speedup over a classical computer. This chapter is focused on the generation of states with Wigner negativity, and will summarize the results and methods used in the corresponding appended papers. Specifically, Section 2.2 deals with states that propagate in a transmission line (Papers A-D), while Section 2.3 is about preparation of states confined inside a cavity (Paper E). First, I briefly introduce the theoretical formalism of open quantum systems which is needed to model both of these systems.

2.1 Open quantum systems

A quantum system—for example, a qubit or cavity—is never completely isolated, but rather coupled to its environment[1]. This means information and energy can leak from the system and be lost to the environment. The evolution of this type of system is not only generated by the Hamiltonian, the leakage into the environment must also be included. For now, we only consider radiative decay, meaning photons decay from the system into the environment. Under certain assumptions[2], the time-evolution of the system state ρ is obtained by

[1] The environment is sometimes also called a *bath* or *reservoir*, and is assumed to have many more degrees of freedom than the system.

[2] We assume the system is weakly coupled to the environment and has a negligible influence on it (Born approximation), and that only the current state of the system is needed to predict the future state (Markov approximation).

solving the Lindblad master equation [47]

$$\frac{\mathrm{d}\rho}{\mathrm{d}t} = -\mathrm{i}\,[H,\rho] + \gamma\mathcal{D}[\hat{c}]\rho. \tag{2.1}$$

The first term on the right-hand-side simply gives the von Neumann equation for the Hamiltonian evolution of a closed system. The second term introduces dissipation with decay rate γ. The action of the dissipation superoperator[3] $\mathcal{D}$ is defined as $\mathcal{D}[\hat{c}]\rho = \hat{c}\rho\hat{c}^\dagger - \hat{c}^\dagger\hat{c}\rho/2 - \rho\hat{c}^\dagger\hat{c}/2$, where $\hat{c}$ is the annihilation operator of the system in question. For an electromagnetic field state in a lossy cavity it would be the bosonic operator $\hat{a}$ which we have already encountered, and for a qubit it would be the pseudo-spin[4] lowering operator $\sigma_- = (\sigma_x + \mathrm{i}\sigma_y)/2$.

2.2 Propagating states

Generating Wigner-negative states in the laboratory is a nontrivial endeavor. We wished to investigate whether Wigner negativity could be obtained from the output of two of the simplest and most well-known systems in quantum optics: a two-level system (qubit) and a nonlinear cavity, both driven by classical fields. Both systems are known to have the ability to produce transient Wigner-negative states, but we are interested in the steady-state with a continuous drive.

The two systems are illustrated in Fig. 2.1. The two-level system at the end of a semi-infinite transmission line is the focus of Section 2.2.1, and the nonlinear cavity is presented in Section 2.2.2. The transmission line that is coupled to the qubit or cavity constitutes the environment into which the respective system may decay into. Since we are not interested in the systems themselves, but rather their output into the transmission line, we cannot simply solve the master equation (2.1). Different methods were used to obtain the output state of each system, and they will be presented in the corresponding sections. But first, we must define a state from the steady-state output field.

Defining an output mode

As opposed to a cavity, a transmission line can host a continuum of modes which are no longer identified by a discrete index n as in Section 1.3, but by the continuous frequency ω. We will work in the time domain, and the corresponding field operator is obtained by Fourier transform:

$$\hat{a}(t) = \frac{1}{\sqrt{2\pi}} \int \hat{a}(\omega) e^{\mathrm{i}\omega t}\,\mathrm{d}\omega. \tag{2.2}$$

In steady-state with a continuous drive, the output will also be a continuous stream of photons, so to get a well-defined state containing a finite number of

[3] A superoperator maps operators to operators.
[4] The operators σ_x and σ_y are Pauli spin matrices.

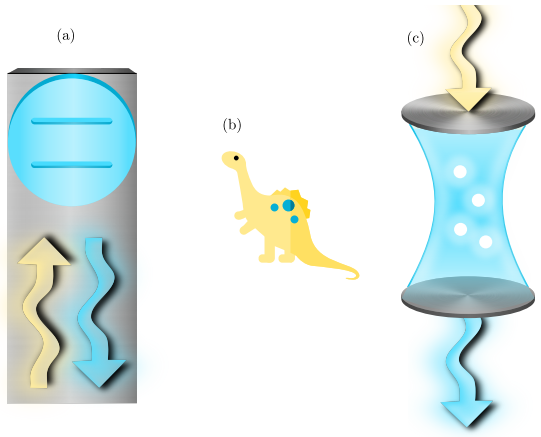

Figure 2.1: (a) Qubit at the end of a transmission line which acts as a mirror. The yellow arrows represent the classical drive field, and the blue arrows represent the emitted quantum radiation field. (b) A dinosaur to indicate that the systems (a) and (c) are not new inventions. (c) Kerr cavity illustrated as an optical cavity, but it can be another type of system, for example superconducting circuits.

photons the field must be filtered to create a wavepacket [9, 48]. A temporal mode function $f(t)$ defines the temporal profile of a wavepacket [49]. Assuming it is nonzero only within some finite time range $[0, T]$, the annihilation operator for this particular wavepacket is then expressed as

$$\hat{A}_f = \int_0^T f(t)\hat{a}(t)\,\mathrm{d}t. \tag{2.3}$$

The mode function must be normalized, i.e. $\int_0^T |f(t)|^2\,\mathrm{d}t = 1$, for the operators to fulfill the bosonic commutation relation $[\hat{A}_f, \hat{A}_f^\dagger] = 1$. Then the wavepacket represents a bosonic quantum state. We found that the Wigner-negativity of an output state from both systems is heavily dependent on the mode function. This will be expanded on in Section 2.2.3.

2.2.1 Qubit in front of a mirror

A two-level system, or qubit, illuminated by a monochromatic classical electromagnetic field is arguably the simplest model of light-matter interaction. Here we consider a single transmission line which is coupled to the qubit. This transmission line hosts both the field incident to the qubit and the field emitted by it, as shown in Fig. 2.1(a). When the drive field is on resonance with the qubit it will be excited. The excited qubit will in turn decay by spontaneous emission into the transmission line. This emission is called *resonance fluorescence*.

It is an old and well-studied phenomenon, observed already in 1969 [50] and explained in 1976 [51]. Resonance fluorescence is known to exhibit nonclassical properties such as antibunching and squeezing [52–54]. Still, a characterization in terms of the Wigner function had not been previously performed.

Numerical methods

To obtain the state of the radiation field, we simulated homodyne measurements of it. Since measurement results of quantum systems are stochastic in nature, the equation for a quantum system that is continuously monitored in time is a *stochastic master equation* [55]:

$$\mathrm{d}\rho(t) = -\mathrm{i}[H, \rho(t)]\,\mathrm{d}t + \gamma\mathcal{D}[\sigma_-]\rho(t)\,\mathrm{d}t + \mathcal{H}[e^{-\mathrm{i}\theta}\sigma_-]\rho(t)\,\mathrm{d}W(t). \tag{2.4}$$

The two first terms on the right-hand-side correspond directly to the deterministic master equation (2.1), where the leftmost term gives the Hamiltonian evolution. Working in the rotating frame of the qubit and applying the rotating wave approximation, the Hamiltonian only contains a drive term with classical drive strength Ω:

$$H = -\mathrm{i}\sqrt{\gamma}\Omega(\sigma_+ - \sigma_-). \tag{2.5}$$

The factor $\sqrt{\gamma}$ represents the coupling to the transmission line. The rightmost term in Eq. (2.4) is the stochastic part which represents the back-action of the measurement process on the system. For homodyne detection, the superoperator defining the measurement process is [55]

$$\mathcal{H}[c]\rho = c\rho + \rho c^\dagger - \mathrm{Tr}\left[(c + c^\dagger)\rho\right]\rho. \tag{2.6}$$

The phase $e^{-\mathrm{i}\theta}$ denotes the phase of the local oscillator as described in Section 1.5.3. The measurement term is accompanied by the stochastic increment $\mathrm{d}W$ called the Wiener increment[5], which is given by a normally distributed random variable. Since stochastic processes are often not differentiable[6], integrals of stochastic differential equations cannot be interpreted in the usual way. For this reason, one cannot in general take a numerical method for solving ordinary differential equations and apply it to stochastic differential equations [56]. To solve Eq. (2.4), I implemented the simplest applicable numerical scheme, called Euler-Maruyama, and the second simplest, the Milstein method [56]. I found no difference between the performance of the two methods except that sometimes Milstein could converge with larger time-steps than Euler-Maruyama.

Still, Eq. (2.4) gives the time evolution of the qubit conditioned on measurement outcomes, but we do not only want the qubit state but also its output field. With this method we also get an expression for the measurement signal proportional to the field quadrature decided by the phase θ. When filtering with a real-valued mode function $f(t)$, the equation for the signal is

$$\mathrm{d}j(t) = \frac{f(t)}{\sqrt{2}}\left(\sqrt{\gamma}\mathrm{Tr}\left[(e^{-\mathrm{i}\theta}\sigma_- + e^{\mathrm{i}\theta}\sigma_+)\rho(t)\right]\mathrm{d}t + \mathrm{d}W(t)\right). \tag{2.7}$$

[5]The Wiener process is a stochastic process often called *Brownian motion*.
[6]In particular, the Wiener process is nowhere differentiable.

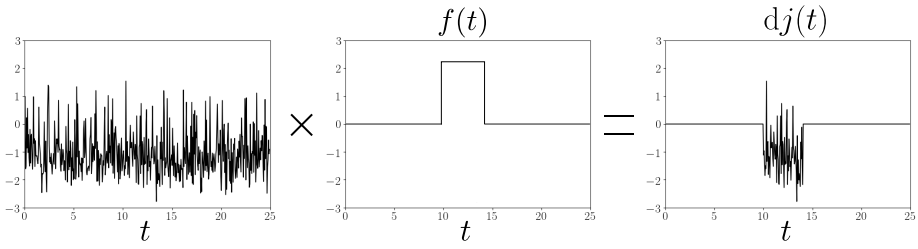

Figure 2.2: The simulated homodyne current (left) is filtered by a function $f(t)$ (middle) to produce the measured signal $\mathrm{d}j(t)$ (right).

For simplicity we used a boxcar filter as depicted in the middle panel of Fig. 2.2. The signal is integrated over the measurement time T, and the procedure is repeated a few thousand times to construct histograms of the integrated signals. All of this is done for around 20 uniformly spaced angles in the range $[0, \pi]$ to gain sufficient information to reliably reconstruct the underlying state [11]. The reconstruction was performed with a *Maximum Likelihood* method. Maximum likelihood estimation is a classical inference method that has been generalized to quantum state estimation [57, 58]. In essence, it is an iterative method that aims to find the state that maximizes the likelihood to obtain the data that was actually observed[7]. An overview of the whole procedure from simulation to state estimation is illustrated in Fig. 2.3. Finally, the Wigner function of the state is calculated from the density matrix. It is expressed in the Fock basis and can be written as

$$\rho = \sum_{m,n} \rho_{mn} \left|m\right\rangle \left\langle n\right| . \tag{2.8}$$

Inserting this into Eq. (1.9) gives

$$W(x,p) = \sum_{m,n} \rho_{mn} W_{mn}(x,p), \tag{2.9}$$

where

$$W_{mn}(x,p) = \frac{1}{2\pi} \int_{-\infty}^{\infty} \mathrm{d}y \, e^{-\mathrm{i}py} \left\langle x + \frac{y}{2} | m \right\rangle \left\langle n | x - \frac{y}{2} \right\rangle . \tag{2.10}$$

We use the fact that the overlap between Fock eigenstates[8] $|n\rangle$ and quadrature eigenstates $|x\rangle$ is given by the harmonic oscillator eigenfunctions in the position basis [59]:

$$\langle x|n\rangle = \frac{1}{\sqrt{2^n n!}} \left(\frac{1}{\pi}\right)^{1/4} e^{-x^2/2} H_n(x), \tag{2.11}$$

[7] An alternative state estimation method will be presented in Section 3.2.

[8] Fock states are also known as number states. $|n\rangle$ is a state with n photons.

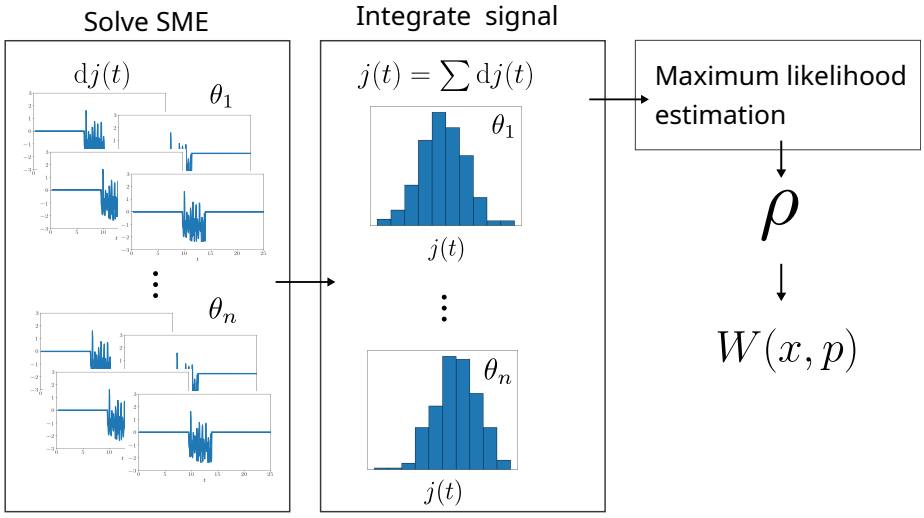

Figure 2.3: The stochastic master equation (SME) (2.4) is solved to obtain simulated measurement signals (2.7). This is performed a couple of thousand times per homodyne angle, the signals are integrated and the results are binned to form histograms. The measurement statistics are then used to reconstruct the density matrix ρ with maximum likelihood estimation. Then the Wigner function is calculated from Eqs. (2.9)–(2.12).

where H_n denotes the nth Hermite polynomial. After some calculation, this gives

$$\begin{cases} W_{mn} = \frac{1}{\pi} e^{-(x^2+p^2)} (-1)^m \sqrt{\frac{m!}{n!}} (2x^2+2p^2)^{\frac{n-m}{2}} e^{\mathrm{i}(n-m)\phi} L_m^{n-m}(2x^2+2p^2), & n \geq m, \\ W_{mn} = \frac{1}{\pi} e^{-(x^2+p^2)} (-1)^n \sqrt{\frac{n!}{m!}} (2x^2+2p^2)^{\frac{m-n}{2}} e^{\mathrm{i}(m-n)\phi} L_n^{m-n}(2x^2+2p^2), & n < m, \end{cases} \tag{2.12}$$

where L_m^{n-m} are associated Laguerre polynomials.

In Paper A we used these methods to demonstrate that for certain parameter regimes the emission from an ideal qubit in front of a mirror is indeed characterized by a negative Wigner function.

Additional decay channels

In Paper B we added realistic imperfections to the system, specifically pure dephasing and nonradiative decay of the qubit. This was done by adding the following terms to the right-hand-side of the stochastic master equation (2.4):

$$\Gamma_n \mathcal{D}[\sigma_-]\rho + \Gamma_\varphi \mathcal{D}[\sigma_z]\rho, \tag{2.13}$$

where Γ_n is the nonradiative decay rate and Γ_φ is the pure dephasing rate. We used decoherence rates typical for a circuit-QED setup, and found that Wigner

negativity was still present in the output, albeit slightly reduced. This indicated that an experimental realization was feasible.

Experimental realization
Paper C was a circuit-QED experimental implementation of the system by Yong Lu, former PhD student at Chalmers. The results agreed well with simulations as shown in Fig. 2.4. State tomography was performed with a variation of Maximum likelihood, to be revisited later in Section 3.2.2.

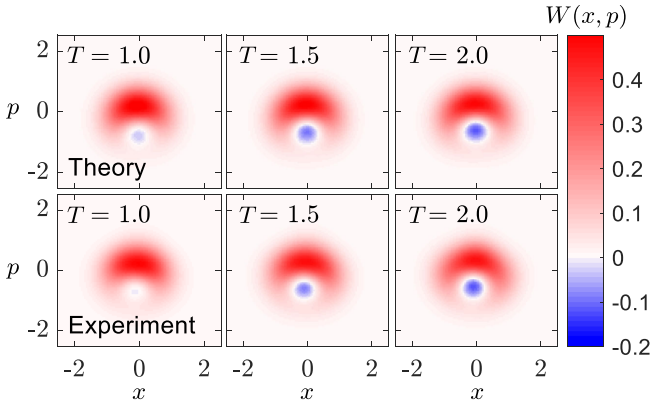

Figure 2.4: Wigner functions from simulations and experiments for different lengths T of the boxcar filter (in units of the decay rate γ).

2.2.2 Kerr parametric oscillator

The cavity system is illustrated in Fig 2.1(c). It is drawn as an optical cavity, but the same type of system can also be created using superconducting circuits. Then the Kerr effect originates from the Φ^4-term in the expansion of the Josephson inductance in a superconducting circuit [cf. Eq. (1.14)], and this nonlinearity can be used to obtain Wigner negativity.

The Hamiltonian of our system is

$$H = \underbrace{A\hat{a}^2 + A^*\hat{a}^{\dagger 2}}_{H_{\text{drive}}} + \underbrace{K\hat{a}^{\dagger 2}\hat{a}^2}_{H_{\text{Kerr}}}. \tag{2.14}$$

First is the parametric drive term which can be interpreted as a two-photon drive, where the classical drive[9] with amplitude A is converted into pairs of photons. The coherence between photon pairs turns out to be important for the negativity, but I will not go into details here. A slightly more in-depth explanation of such a parametric effect will come later in Section 3.1.2. The second term represents the Kerr nonlinearity of strength K.

[9]It is assumed that the drive field has very many photons and is never depleted.

In quantum optics, a linear parametric oscillator with Hamiltonian H_{drive} is known to create squeezed states, which are states exhibiting quadrature fluctuations below the vacuum level. In steady-state the maximum attainable squeezing inside a parametric oscillator is equal to 50 % of the vacuum noise. Interestingly, there is no such limitation to the squeezing of the output field [60]. However, while squeezed states are quantum in the sense that they cannot be explained by classical physics, they are Wigner-positive. As mentioned in Chapter 1, a higher order nonlinearity is needed for Wigner negativity. When the Kerr-nonlinearity is added to the parametric nonlinearity, so-called Schrödinger's cat states[10] can be generated in the cavity [61]. When the system suffers single-photon loss, which is often the strongest loss mechanism, the cat state is only transient and the Wigner-negativity disappears even if the system is continually driven [62]. So it is well-known that the intra-cavity state is Wigner-positive in steady-state [63, 64]. Inspired by the fact that squeezing properties can be different between the cavity field and its corresponding output field, we investigated whether it is possible to obtain a Wigner-negative *output* state from a Kerr parametric oscillator, and the answer is yes.

Optical media can only provide weak nonlinearities, and this is very often used as an argument in favor for superconducting circuits where a Josephson junction can provide strong nonlinearity. However, we find from simulations that a weak Kerr nonlinearity is sufficient to create Wigner-negativity in the leaked output field.

Numerical method

Here a new method is used, which is a lot more efficient than repeatedly solving a stochastic master equation and then inferring the state via maximum likelihood estimation. It was not available during our project on resonance fluorescence as the theory was published in 2019 [65]. With this method, the model of the system is augmented by a fictitious cavity mode that represents the propagating output state in a particular temporal mode defined by the wave packet shape $f(t)$. The virtual cavity is assigned bosonic operators $\hat{v}$, $\hat{v}^\dagger$, and is coupled to the Kerr-cavity with a time-dependent coupling $g_f(t)$ which is calculated from $f(t)$ as

$$g_f(t) = \frac{f^*(t)}{\sqrt{1 - \int_0^t dt' \left|f(t')\right|^2}}. \tag{2.15}$$

In the following we will assume $f(t)$ to be real. Then, if $\hat{a}$ is the Kerr-cavity annihilation operator, a term $0.5\mathrm{i}\sqrt{\kappa}g_f(t)(\hat{v}\hat{a}^\dagger - \hat{v}^\dagger\hat{a})$ is added to the Hamiltonian, where κ is the single-photon loss rate of the Kerr-cavity. An effective master equation for the two cavity modes is obtained by also adding a time-dependent damping term $g_f(t)\mathcal{D}[\hat{v}]\rho$ to the master equation (2.1). The modified equation is then

$$\frac{\mathrm{d}\rho}{\mathrm{d}t} = -\mathrm{i}\,[H,\rho] + \kappa\mathcal{D}[\hat{a}]\rho + g_f(t)\mathcal{D}[\hat{v}]\rho + 0.5\mathrm{i}\sqrt{\kappa}g_f(t)(\hat{v}\hat{a}^\dagger - \hat{v}^\dagger\hat{a}). \tag{2.16}$$

[10] We will encounter cat states again in Section 2.3.

This equation for the composite system of cavity and output can then be solved with standard methods, and the output state obtained by taking the partial trace. We used QuTiP [66] for these calculations. An example of results is displayed in Fig. 2.5.

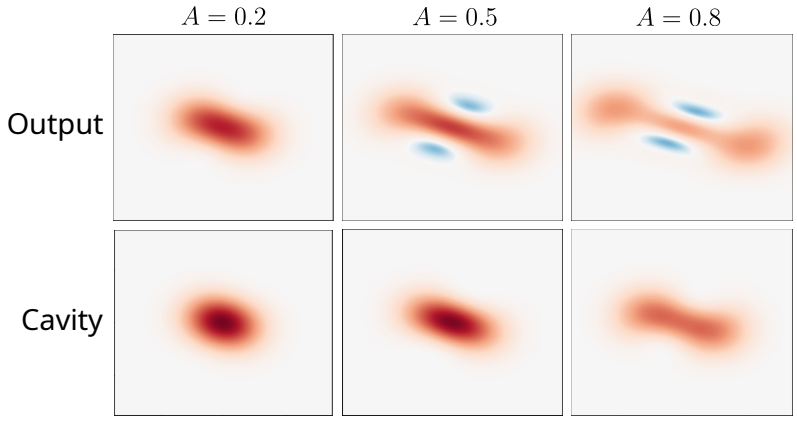

Figure 2.5: Top row: Wigner functions of the leaked output state for a boxcar filter $T = 5$ and Kerr nonlinearity $K = 0.5$ for different drive strengths A (in units of the decay rate κ). Bottom row: Wigner function of the corresponding steady-state intracavity states. The cavity states become more squeezed with stronger drive but remain positive. On the contrary, the output field can display Wigner-negativity as indicated by the blue regions.

2.2.3 Wigner negativity of different wavepacket shapes

At the beginning of this chapter it was explained that the continuous field must be filtered into a wavepacket to select a single-mode bosonic state out of the continuum, and that the Wigner negativity of the state is heavily reliant on the shape of the wavepacket which is defined by the mode function $f(t)$. This is the case for both the qubit in front of a mirror and the Kerr cavity. We quantify the amount of negativity by the Wigner Logarithmic Negativity (WLN) [67]

$$\mathsf{WLN} = \log\left(\int |W(x,p)|\,\mathrm{d}x\,\mathrm{d}p\right). \tag{2.17}$$

There is an infinite number of possible mode functions, since the only requirement is that it is normalized such that

$$\int_0^T |f(t)|^2\,\mathrm{d}t = 1. \tag{2.18}$$

For simplicity we started with a so-called boxcar filter, which is illustrated in Fig. 2.6(a). This function is zero until we have determined we are in steady-state, then it jumps to a constant value for some time T after which it returns

to zero. For this function, the time T is essentially the observation time, during which we measure all emission from the system. We also tried a Gaussian shaped function, also illustrated in Fig. 2.6(a). Interestingly, for optimized drive strengths and filter widths the Gaussian filter gives around twice as much Wigner-negativity as the boxcar, as shown in Fig. 2.6(b) and Fig. 2.6(c). The former shows the Wigner negativity for a range of drive strengths for optimized filter widths with the Kerr cavity, and the latter shows the maximum WLN for both systems.

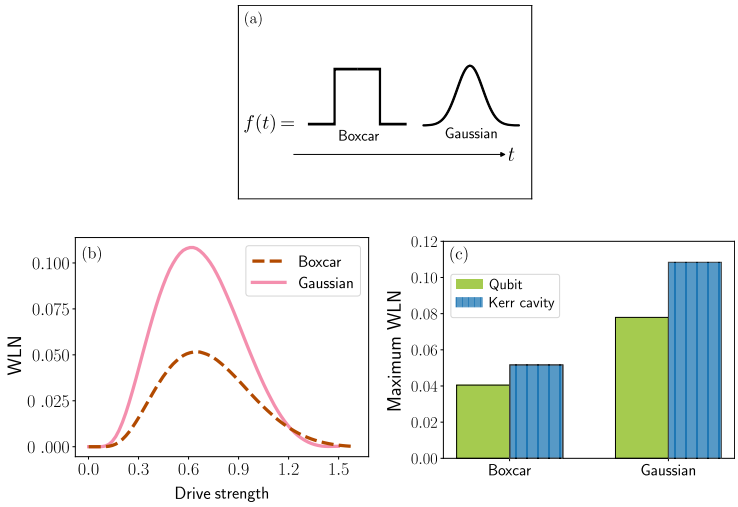

Figure 2.6: Mode function shape dependence of Wigner negativity. (a) Two different mode functions, boxcar and Gaussian. (b) WLN as a function of drive strength with optimized filter widths for the Kerr cavity. (c) Maximum WLN for the qubit in from of a mirror, and Kerr cavity for both mode functions. It is clear that the Gaussian filter results in a lot more negativity.

We tried other mode functions shapes such as Lorentzian, but that gave even less negativity than the boxcar. An attempt to determine the optimal mode function was made with brute-force optimization. A randomized mode shape was initialized, and the optimizer `SLSQP` from `scipy.optimize` [68] was used to maximize WLN under the constraint of normalization, and that the first and final values were zero. The result is shown in Fig. 2.7, and is fitted nicely with a Gaussian curve. This is not a guarantee that the Gaussian is the best, but a strong indicator. The reason why this is the case is still an open question.

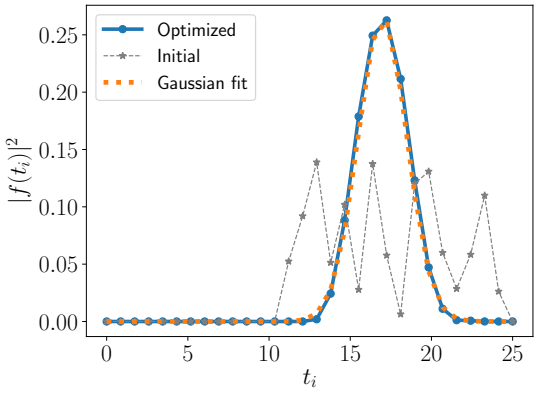

Figure 2.7: Numerical optimization of the wavepacket shape at discrete time points t_i. In order to ensure the system is in steady-state, filtering starts after $t_i > 10$. The initial mode shape was generated by random numbers (gray stars). The values were then optimized for maximum WLN (blue dots). A Gaussian curve can be well fitted to the optimized shape (orange dashed line).

2.3 Cavity states

As opposed to propagating states that are unconfined in the direction of propagation, the states described in this section are confined in all spatial directions by a cavity. Since quantum information is exceptionally vulnerable to environmental noise and experimental imperfections, quantum error correction will play an important role for future large-scale quantum computers [69]. Error correction codes use additional degrees of freedom to redundantly encode information, and for discrete-variable systems consisting of regular qubits this corresponds to adding more qubits to the system. But since continuous variable states have an infinite Hilbert space by themselves, the idea is to encode qubits in electromagnetic cavity states. The most popular bosonic codes use states called binomial states [70], cat states [71], and GKP states [72] which are highly nonclassical states as can be inferred from their negative Wigner functions as shown in Fig. 2.12. In Paper E we generate such microwave states in a single-mode three-dimensional[11] superconducting cavity. Below, I first present some important properties of the system before explaining the method.

2.3.1 The system

The linear cavity is coupled to a qubit for the required nonlinearity, as illustrated in Fig. 2.8. The system of a qubit coupled to a cavity is described by the

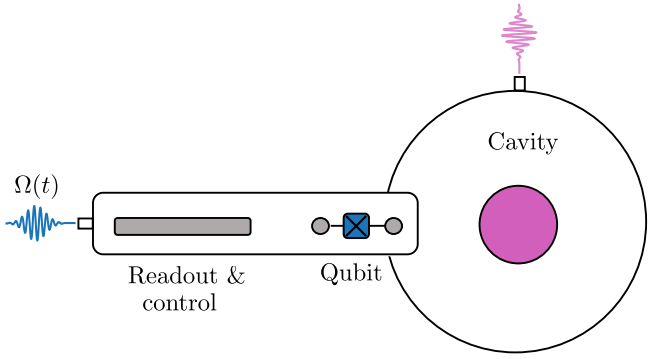

Figure 2.8: Top view schematic of the qubit-cavity system from Fig. 1.8(b), where a transmon qubit is capacitively coupled to a 3D microwave cavity resonator. Readout and driving of the qubit is done via an additional planar resonator.

Jaynes-Cummings Hamiltonian [73]

$$H_{\mathrm{JC}} = \frac{\omega_q}{2}\hat{\sigma}_z + \omega_c \hat{a}^\dagger \hat{a} + g(\hat{a}\hat{\sigma}_+ + \hat{a}^\dagger \hat{\sigma}_-). \tag{2.19}$$

[11] 3D cavities generally have longer coherence times than planar resonators.

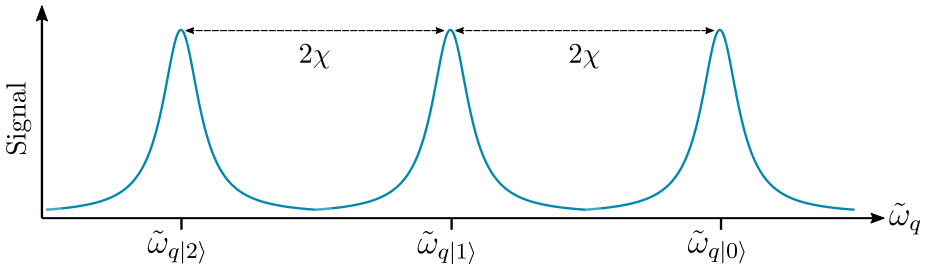

Figure 2.9: An illustration of photon-number resolved spectroscopy by probing the qubit resonance frequency f_q, which is indicated on the x-axis. Peaks indicate resonance frequencies separated by 2χ for 0, 1 and 2 photons in the cavity, respectively. In a real spectrum, the peak amplitudes would proportionally correspond to the photon populations.

The leftmost term describes a qubit with transition frequency ω_q, and the middle term represents the harmonic oscillator modeling the cavity with resonance frequency ω_c. The final term gives the interaction between the two systems, with interaction strength g. The difference between the qubit and cavity resonance frequencies is called the *detuning* $\Delta = |\omega_q - \omega_c|$. For weak coupling g and large detuning Δ the *dispersive approximation* can be made, which entails a perturbative expansion of the Jaynes-Cummings Hamiltonian to second order in $g/\Delta \ll 1$ that gives the dispersive Hamiltonian

$$H = \frac{\tilde{\omega}_q}{2}\hat{\sigma}_z + \omega_c \hat{a}^\dagger \hat{a} + \chi \hat{a}^\dagger \hat{a} \hat{\sigma}_z, \tag{2.20}$$

where $\tilde{\omega}_q = \omega_q + \chi$ is the Lamb-shifted qubit frequency and $\chi = g^2/\Delta$ is the dispersive coupling strength, also called the dispersive shift. We can suggestively rewrite this Hamiltonian as

$$H = \omega_a \hat{a}^\dagger \hat{a} + \frac{1}{2}(\tilde{\omega}_q + 2\chi \hat{a}^\dagger \hat{a})\hat{\sigma}_z. \tag{2.21}$$

From this expression it is clearly seen that the qubit frequency is shifted[12] by 2χ for each photon in the cavity. When the shift per photon dominates over the decay rates of the system, $2\chi \gg \gamma, \kappa$ the system is said to be in the *strong dispersive* regime [74]. In this regime, the qubit transition energy can be resolved into separate spectral lines for each photon number state of the field as is sketched in Fig. 2.9.

2.3.2 Universal gate set

The photon-number resolving property is important in order to be able to control the system conditioned on the number states of the cavity. One such oper-

[12]This can be interpreted as a Stark shift of the qubit.

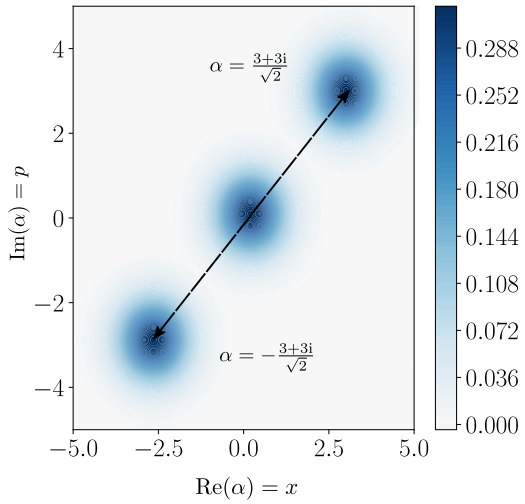

Figure 2.10: The Wigner functions of the vacuum state (at the origin) displaced in two different directions.

ation is the SNAP (selective number-dependent arbitrary phase) gate [75], which together with simple displacements of the cavity field provides universal control of the cavity [76]. This means that an arbitrary unitary operation can be decomposed in terms of these two operations which are described below.

Displacements
The displacement operation

$$D(\alpha) = \exp(\alpha \hat{a}^\dagger - \alpha^* \hat{a}), \tag{2.22}$$

simply moves a state in phase space with the distance and direction set by the complex parameter α, as illustrated in Fig. 2.10. It is implemented experimentally by applying a classical microwave drive on the cavity, which generates a displacement corresponding to the time-integral of the drive amplitude.

Selective number-dependent arbitrary phase (SNAP) gate
The SNAP gate applies different phases to different photon-number states of the cavity, with the unitary operator

$$S(\vec{\theta}) = \prod_{n=0}^{N} e^{i\theta_n |n\rangle\langle n|}, \tag{2.23}$$

where the vector $\vec{\theta} = (\theta_0, \theta_1, \ldots, \theta_N)$ contains the phase angles for each number state up to some truncation N. The experimental implementation of this gate is discussed soon in Section 2.3.3.

Arbitrary unitary operations

As mentioned before, the combination of arbitrary displacements and SNAPs enable universal control of the cavity field. Any unitary can be expressed as a sequence of alternating displacements and SNAPs:

$$U = D(\alpha_1)S(\vec{\theta}_1)D(\alpha_2)S(\vec{\theta}_2)D(\alpha_3)\dots \tag{2.24}$$

We use a gradient descent method to optimize displacement parameters α and SNAP angles $\vec{\theta}$ for a chosen length of the sequence (2.24), which we choose to contain between two and three SNAPs depending on which target state is to be generated. A target state with a higher photon number generally needs a longer sequence to achieve high fidelity, but it also cannot be made too long depending on the coherence time[13] of the system.

2.3.3 Experimental implementation and optimal control

In our setup, cavity displacements can be implemented by applying a simple, short pulse to the cavity. The SNAP is not as straightforward. To apply a phase to number state $|n\rangle$, a drive $\Omega_n(t)$ can be applied at the corresponding qubit frequency $\tilde{\omega}_q - 2\chi n$ (see Fig. 2.9). To apply multiple phases, many such drives for different n can be superposed [75]. However, since the the bandwidth of an applied pulse is inversely proportional to the duration, pulses must be sufficiently long in time in order to not overlap more than one resonance in Fig. 2.9. For us, the required time is too long compared to the coherence time of our system. In order to obtain shorter SNAP pulses we used *optimal control*. Optimal control was developed already in the 1950s for classical systems, as many engineering problems are naturally posed as optimal control problems[14]. The problem formulation is to find a control function for the dynamical system such that a cost function is optimized [77].

Now, *quantum* optimal control [78] has emerged as a whole research field by itself. It is interesting but complicated, and people write whole dissertations [79–85] on this topic alone. For this reason we utilized the available software toolkit Boulder Opal from Q-CTRL [86] to perform the optimizations. The goal is to find an optimized time-dependent Hamiltonian $H_{\text{opt}}(t)$ that generates the time-evolution $U_{\text{opt}}(t) = e^{-\mathrm{i}H_{\text{opt}}t}$ such that the at the final time T, the optimized evolution is equal to the target unitary: $U_{\text{opt}}(T) = U_{\text{target}}$. In our case, the target is a SNAP gate: $U_{\text{target}} = S(\vec{\theta})$. The cost function to be optimized is the fidelity to the target unitary. We optimize a single complex amplitude $\Omega(t)$ for the qubit drive Hamiltonian $H_d(t) = \Omega(t)\hat{\sigma}_- + \Omega^*(t)\hat{\sigma}_+$. An optimized pulse is shown in Fig. 2.11. As can be seen, the shape is rather complicated.

[13] The coherence time is how long a system can maintain a quantum state.

[14] For example: find the time-optimal motion for an industrial robot to move a component.

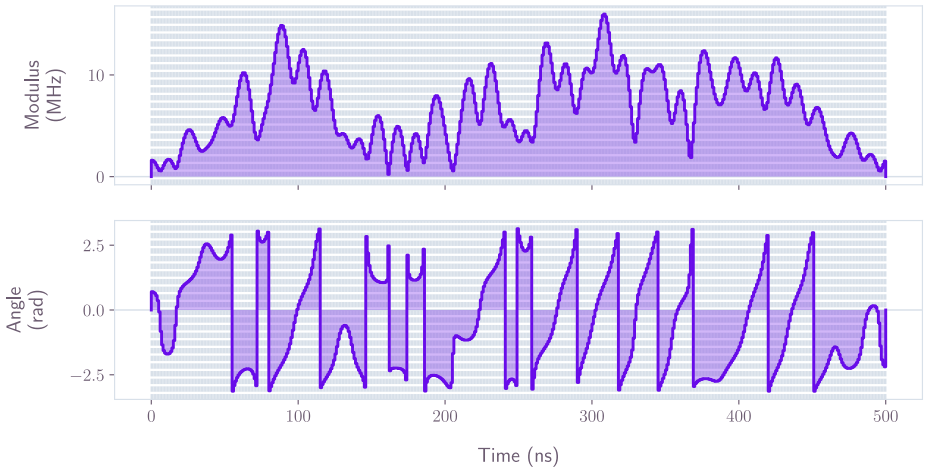

Figure 2.11: Amplitude and phase of the optimized qubit drive implementing a `SNAP` gate in 500 ns.

Results

Several types of states were successfully produced in the experiment performed by Marina Kudra, PhD student at Chalmers. Measurements of the Wigner functions were performed, and results from Paper E are displayed in Fig. 2.12. It shows a Fock state $|2\rangle$, instances of binomial-, cat- and GKP-code states,

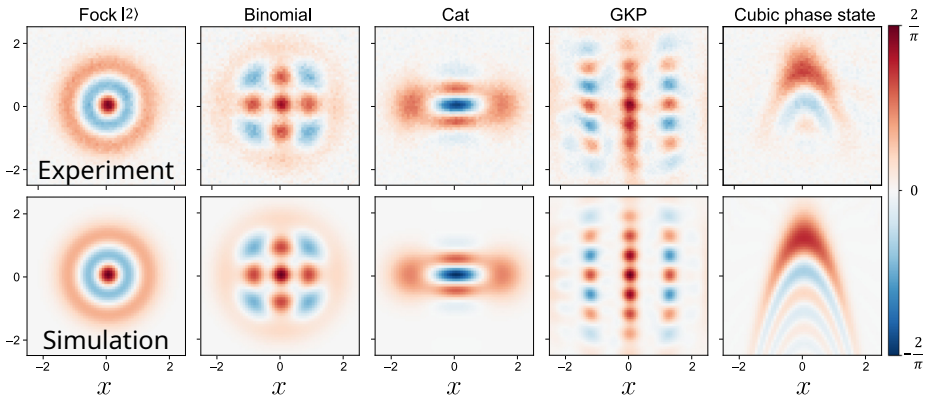

Figure 2.12: Wigner tomography measurements (top row) of generated bosonic states inside the 3D cavity, compared with simulations (bottom row). Blue indicates Wigner-negativity.

and a *cubic phase state*. This last state is particularly notable, since this is the first time such a state has been generated after many years of efforts in

the quantum optics community [87]. As mentioned in Chapter 1.4, at least a cubic nonlinearity is needed for a quantum operation to provide universality. The cubic phase *state* can be used to perform a cubic phase *gate* via gate teleportation [88], and this is sufficient to provide universal control together with Gaussian states and operations.

Chapter 3

Quantum state characterization

In the previous chapter I discussed quantum state generation. Whether we want to simply observe what type of states are created by the system, as in Papers A-D, or if there are particular target states, such as in Paper E, there is a need to ascertain which state was actually created. This can only be done by analyzing measurements of the prepared state. The density matrix of the state can then be reconstructed based on the measurement data. This procedure is called quantum state reconstruction, estimation, or *tomography*, due to the problem being similar to medical tomography as illustrated in Fig 3.1. Single-mode CV state tomography is the topic of Paper G, to be discussed further in Section 3.2.

Sometimes a specific property of the state is sought after rather than the density matrix, and in that case full tomography is not needed. Instead, one can construct a so-called *witness* that determines whether the state possesses the sought-after property or not. A prototypical example of such a property is *entanglement* [89], which is a distinct feature of quantum mechanics. In Paper F, the entanglement structure of a multimode microwave state is investigated. This is presented right below in Section 3.1.

3.1 Multimode entanglement

Entangled states play an essential role in quantum information theory, where they enable quantum teleportation [90] and act as a resource for quantum cryptography [91, 92], quantum metrology [93, 94] and quantum communication [95]. Entangled states can also be utilized in quantum computing. In the circuit model of quantum computing described in Section 1.4, single modes are sequentially acted on by quantum operations and at the end measured to obtain an

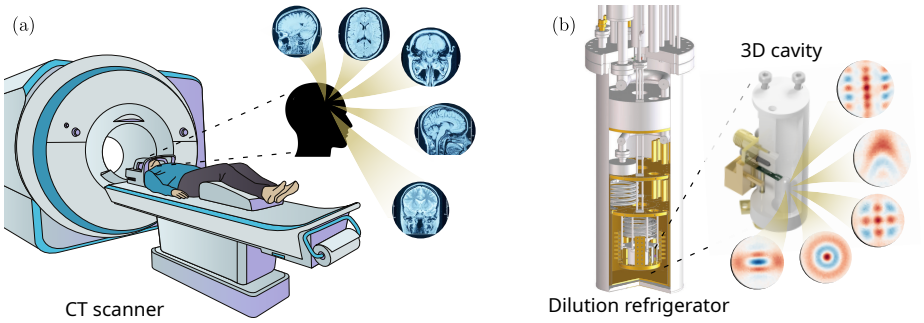

Figure 3.1: (a) CT (computed tomography) scans produces measurement data that is subsequently used to construct images of the brain, which cannot otherwise be (non-invasively) examined as it is hidden inside the skull. (b) Similarly, quantum state tomography is the procedure of determining a quantum state from measurements. In the image, the states are in a cavity inside a cryostat (more specifically, a dilution refrigerator) as in Paper E.

answer to the computation. An interesting alternative is the *measurement-based* model of quantum computing[1], where a specific type of multiparty entangled state known as *cluster state* or *graph state* is prepared, and then quantum information is processed by consecutive measurements on the state [96, 97]. Different types of cluster states are illustrated in Fig. 3.2. Note that linear 1D clusters like Fig. 3.2(a) are not sufficient for universal computing—a 2D state is required for universality.

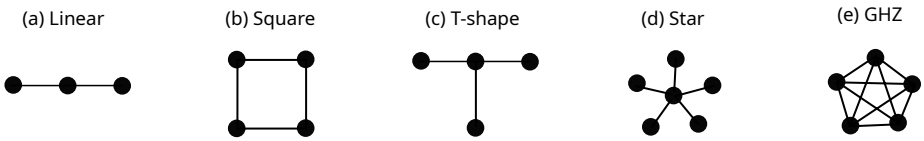

Figure 3.2: Different types of entangled states. Each dot represents a mode, and the lines represent entanglement between modes. (a)-(d) linear, square, T-shaped and star-shaped cluster states. (e) GHZ state [98]. Ideally, these "unit cells" are put together to form larger grids.

Measurement based computations can be performed with qubit- as well as continuous-variable cluster states [99, 100], but continuous-variable platforms have the upper hand in this approach, since many more entangled optical modes have been demonstrated than entangled qubits. While large-scale entanglement with up to a million modes has been generated in the optical regime [101–

[1] Also called one-way quantum computing, because you cannot (deterministically) undo a quantum measurement.

105], multimode entanglement has previously been demonstrated with only three modes in the microwave frequency regime [106]. In Paper F we demonstrate entanglement between seven microwave modes, with the capability to include more in the near future.

3.1.1 Correlation hierarchy for multipartite mixed states

Entanglement between two states (parties) is straightforward to figure out; the state is either entangled or not, i.e. separable. However, the question of entanglement becomes tricky for multipartite states. As can be imagined by looking at Fig. 3.2, entanglement can be distributed in a number of different ways[2] between the different modes. This means there exist several classes of entanglement and separability for multipartite states. As such, entanglement or the absence thereof is characterized as follows. An N-partite mixed state ρ is called *fully separable* if it can be written as a convex combination of product states:

$$\rho = \sum_i p_i \left(\rho_1^i \otimes \rho_2^i \otimes \cdots \otimes \rho_N^i \right), \tag{3.1}$$

where $p_i \geq 0$ and $\sum_i p_i = 1$. This is a direct generalization of the definition of separability for bipartite states ($N = 2$). If a state is not separable it is entangled, but for a multipartite system that does not necessarily mean all parties are equally entangled. One can arrange the N parts (modes) into $k \leq N$ partitions, which are then considered as subsystems. States that are fully separable with respect to this partitioning (or can be written as a mixture of such states) are called *k-separable* [108]. A 2-separable state is often called biseparable. If a state is *not* biseparable, it said to be *genuinely multipartite entangled*. This is because it implies entanglement for any k-partitioning of modes with $k \geq 2$ [109].

For pure states, genuine multipartite entanglement (GME) is equivalent to full *in*separability. When considering mixed states, the situation becomes even more complex. In this context, genuine multipartite entanglement implies full inseparability, but not the other way around [110]. Negating that the state is separable with respect to any of the possible bipartitions individually does not in general eliminate the possibility that the state is a *mixture* of biseparable states. This is sometimes confused in literature [111], and important to keep in consideration for interpreting the results of one of our entanglement tests, which we will get back to in Section 3.1.3.

[2] One can note that there are limitations on how entanglement can be shared. This is called "monogamy of entanglement" [107].

3.1.2 Generation of entanglement

The experiment utilized a Josephson parametric amplifier (JPA) [112] to create entangled microwave modes. The JPA consists of a LC-resonator where a SQUID (described in Section 1.5) provides a tunable inductance. An externally applied magnetic flux is modulated in time to achieve *parametric amplification*. To describe this effect, consider a strong input field at frequency ω_p called the pump, and another field at frequency ω_1 called the signal, interacting in a nonlinear medium. Under certain conditions[3], the interaction between the fields in the nonlinear medium leads to the annihilation of a pump photon and the creation of a signal photon as well as an additional photon called the "idler" with frequency $\omega_2 = \omega_p - \omega_1$ to satisfy energy conservation. The net result is a transfer of pump power to the signal (and idler) [113].

Parametric amplification can be described by classical physics [39, 114], but we are in this case not interested in amplification, but rather in creating nonclassical correlations between different frequency modes. In the absence of a signal field, *spontaneous downconversion* can still occur. This is a quantum phenomenon since it is driven by quantum fluctuations of the vacuum field [115]. In this process, which is illustrated in Fig. 3.3, a single pump photon splits into two highly correlated signal and idler photons at frequencies ω_1 and ω_2. It is natural that the signal and idler photons are correlated since they originate from the same pump photon.

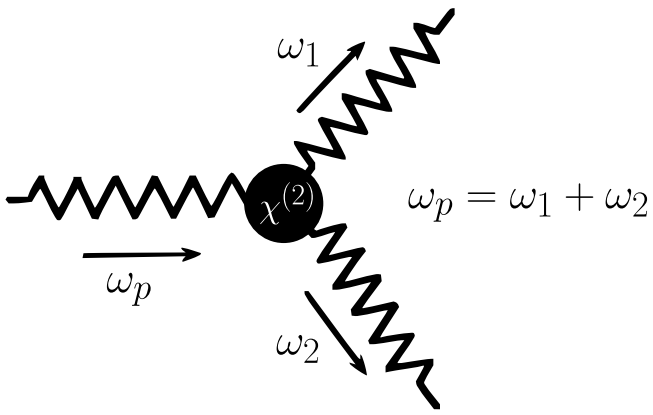

Figure 3.3: Feynman diagram of a three-photon parametric process. The sum of the energy of two photons is equivalent to the energy of the pump photon. Since two photons are generated from a single pump photon, it is intuitively clear that they should be correlated.

When the flux pump is driven at approximately twice the JPA resonance frequency ω_0, correlations will be created between quadratures of frequency modes which are symmetric around half the pump frequency. This is illustrated

[3] Momentum conservation requires a condition called "phase matching".

in Fig. 3.4. As can be seen, one pump generates correlations between separate

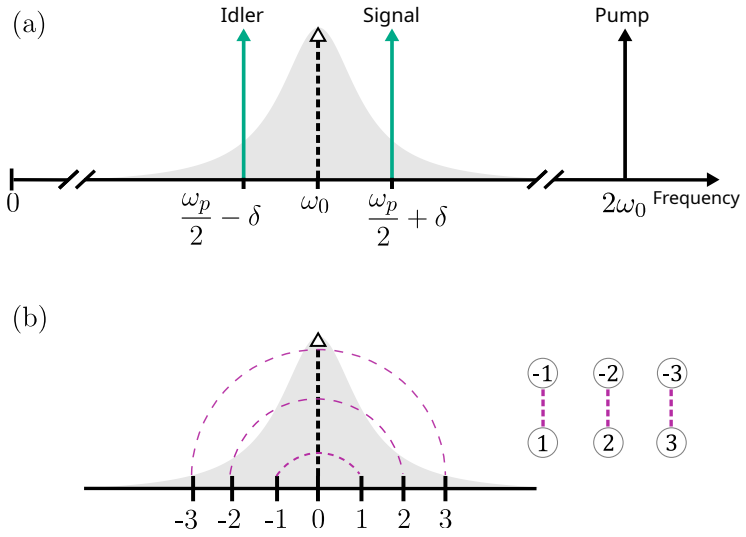

Figure 3.4: (a) A single pump has frequency $\omega_p \approx 2\omega_0$ where ω_0 is the JPA resonance frequency. Correlated signal and idler fields are generated at frequencies $\omega_1 = \omega_p/2 + \delta$ and $\omega_2 = \omega_p/2 - \delta$. (b) We define frequency modes labeled by integers where 0 is the center frequency. Correlations between pairs of signal/idler modes n and $-n$ are generated from the pump as indicated by purple dashed lines. The shaded region indicates the JPA bandwidth.

pairs of modes. In order to generate multimode entanglement, a second pump is added. We define a frequency comb $\omega_n = \omega_0 + n\delta$ with $n = \pm 1, 2, \ldots$ indicating the mode number, and ω_0 is the center frequency as before. Choosing two pumps at frequencies $\omega_{p,1} = 2\omega_{-1} = 2(\omega_0 - \delta)$ and $\omega_{p,2} = 2\omega_1 = 2(\omega_0 + \delta)$, still with total frequency $\omega_{p,1} + \omega_{p,2} = 2\omega_0$, correlations will be generated symmetrically around half the pump frequencies just like with the single pump. This is illustrated in Fig. 3.5. As can be seen, pump 1 generates entanglement between modes -2 and 0, while pump 2 generates entanglement between modes 0 and 2. Thus, correlations between modes -2 and 2 are also generated. This principle generates multimode entanglement.

Note that the inputs to the system consist of a classical drive and vacuum which are both Gaussian, and the interaction is by a second-order nonlinearity, so the resulting multimode state is Gaussian.

3.1.3 Entanglement tests

A Gaussian state is fully characterized by the first and second statistical moments of the quadrature operators [116, 117]. For convenience, the quadrature operators are arranged in a vector $\vec{r} = (\hat{x}_1, \hat{p}_1, \cdots, \hat{x}_N, \hat{p}_N)$ where N is the num-

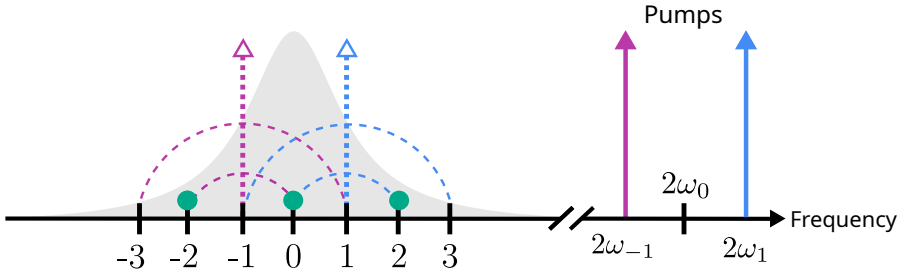

Figure 3.5: Two pumps generate entanglement between different modes. Some of these coincide, for example mode 0 here. Multimode entanglement is then generated as indicated by the green dots.

ber of modes. The first moments are given by the so-called displacement vector which is simply the mean values of the quadratures $\langle \vec{r} \rangle = \mathrm{Tr}\,(\vec{r}\rho)$. The second-order moments construct the $2N \times 2N$ covariance matrix V with elements

$$V_{nm} = \frac{1}{2}\left\langle \{\hat{r}_n \hat{r}_m\} \right\rangle - \langle \hat{r}_n \rangle \langle \hat{r}_m \rangle , \tag{3.2}$$

where the indices m, n run over all $2N$ elements in the vector $\vec{r}$, and $\{\cdot,\cdot\}$ is the anticommutator. Because displacements of multimode systems are just tensor products of local displacements [118] and local displacements have no influence on separability or inseparability of a state [119], we can ignore the displacement vector and consider the covariance matrix only. We can also set $\langle \hat{r}_n \rangle = 0$ for simplicity. As an example, the covariance matrix for a two-mode system could then be expressed as

$$V = \begin{pmatrix} \langle \hat{x}_1^2 \rangle & \frac{1}{2}\langle \{\hat{x}_1, \hat{p}_1\} \rangle & \langle \hat{x}_1 \hat{x}_2 \rangle & \langle \hat{x}_1 \hat{p}_2 \rangle \\ \frac{1}{2}\langle \{\hat{x}_1, \hat{p}_1\} \rangle & \langle \hat{p}_1^2 \rangle & \langle \hat{p}_1 \hat{x}_2 \rangle & \langle \hat{p}_1 \hat{p}_2 \rangle \\ \langle \hat{x}_2 \hat{x}_1 \rangle & \langle \hat{x}_2 \hat{p}_1 \rangle & \langle \hat{x}_2^2 \rangle & \frac{1}{2}\langle \{\hat{x}_2, \hat{p}_2\} \rangle \\ \langle \hat{p}_2 \hat{x}_1 \rangle & \langle \hat{p}_2 \hat{p}_1 \rangle & \frac{1}{2}\langle \{\hat{x}_2, \hat{p}_2\} \rangle & \langle \hat{p}_2^2 \rangle \end{pmatrix} . \tag{3.3}$$

The covariance matrix for 64 modes was measured experimentally. The result can be seen in Fig. 3.6, where it can also be compared to a covariance matrix generated from the theoretical model of the system. Comparing with the matrix (3.3), we understand that nonzero off-diagonal elements in the covariance matrix show correlations between different modes. That does not automatically mean there is quantum entanglement; it could just be classical correlations. So we need to somehow check whether there is entanglement or not. For this we used two different entanglement tests. Before describing those, let us look at the general principle behind an entanglement test or witness, which is illustrated in Fig. 3.7. The set of separable states is a subset of all states, and the witness is an operator $\hat{W}$ that defines a hyperplane that separates a subset of entangled

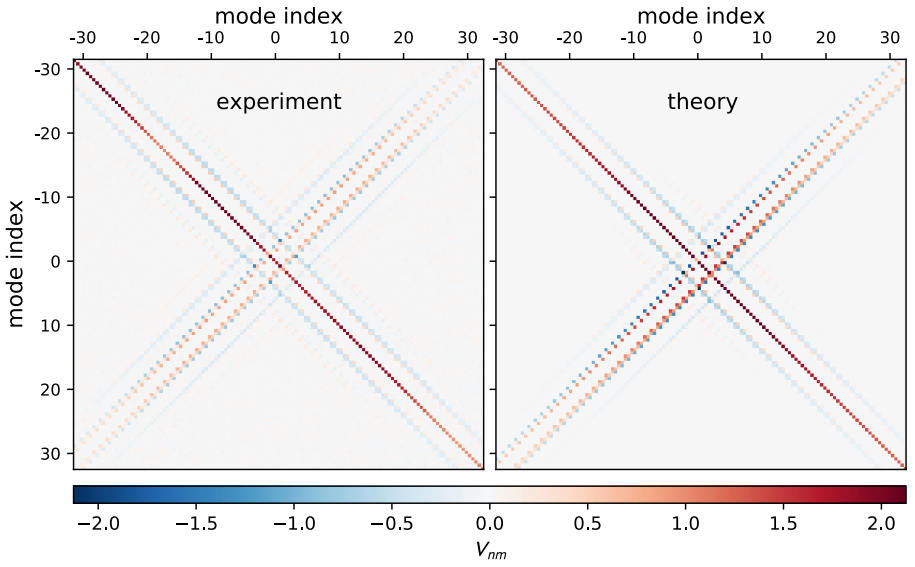

Figure 3.6: There is good agreement between the experimental and simulated covariance matrices for 64 modes. Off-diagonal elements indicate correlations between quadratures of different modes.

and separable states based on its expectation value being positive (separable state) and negative (entangled state). As seen in the figure, non-optimal witnesses can be constructed. This means the witness may recognize some states as entangled, but not all. One can try to optimize the witness [120]. This type of witness indicates entanglement when the inequality $\mathrm{Tr}\,(\rho\hat{W}) > 0$ is violated, but entanglement tests can also be formulated slightly differently.

Entanglement test 1

My co-workers had decided to use an entanglement test from Ref. [121], since it would take measurement errors into account and the measurements were quite noisy. Disregarding this for the time since it only entails scaling by the measurement variance, the test is based on violating the inequality below when the modes are separated into bipartitions I and J:

$$\mathrm{Tr}\,(\vec{h}\vec{h}^{\top}V_{xx}) + \mathrm{Tr}\,(\vec{g}\vec{g}^{\top}V_{pp}) - |(\vec{h}_I, \vec{g}_I)| + |(\vec{h}_J, \vec{g}_J)| \geq 0. \tag{3.4}$$

Here V_{xx} and V_{pp} are the sub-blocks of the covariance matrix that only contain xx and pp correlations, respectively. We also have real-valued column vectors $\vec{h}$ and $\vec{g}$ that construct rank-1 positive-semidefinite matrices $\vec{h}\vec{h}^{\top}$ and $\vec{g}\vec{g}^{\top}$. The elements of these vectors are optimization parameters for a minimization of the expression (3.4). If a negative value is obtained it means that the particular bipartition is inseparable (i.e. entangled). This test is done for all possible

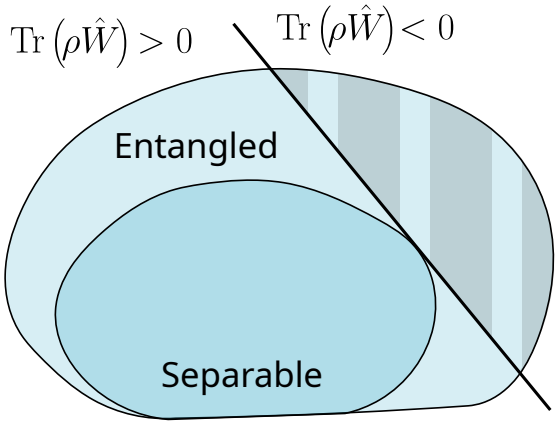

Figure 3.7: Visualization of an entanglement witness $\hat{W}$ that defines a hyperplane at the border between separable and entangled states. Note that having $\mathrm{Tr}\,(\rho\hat{W}) < 0$ with this linear witness is sufficient but not necessary for entanglement. The entire outer region is composed of entangled states, but this witness only recognizes the striped part as such. A corresponding witness can be constructed to use with the covariance matrix instead of the density matrix ρ.

bipartitions of the modes. Taking a subset of seven modes we find negative values for all bipartitions, meaning that the state is fully inseparable. The results in the paper were obtained using differential evolution which is a stochastic optimization method.

Using this test we can only claim full inseparability, not geniune multipartite entanglement (GME). This is because it does not rule out the possibility that the state is a mixture of biseparable states. To claim GME, violations of (3.4) must be obtained for *all* bipartitions with the *same* values of $\vec{h}$ and $\vec{g}$ [111, 122]. Using only four modes from a simulated covariance matrix, I could find such vectors with the naive method of just redoing the stochastic optimization for one of the bipartitions if the resulting $\vec{h}$ and $\vec{g}$ did not also violate the inequality for all other bipartitions. I could not verify GME with the measured covariance matrix, but since simply redoing the optimization if a positive value is observed for any bipartition is an ineffective method that is only expected to find the best $\vec{h}$ and $\vec{g}$ with time and luck, there could very well be GME even if this type of test did not recognize it.

There are also three other problems with this test. First, it assumes there are no xp-correlations, which we actually have. We mitigate this problem by minimizing the correlations with single-mode rotations which do not affect entanglement, but there are always xp-correlations left anyway. Second, there is no guarantee that the stochastic optimization obtains the optimal witnesses $\vec{h}$ and $\vec{g}$. And last but not least, the test is likely not optimal anyhow since we restrict the optimization to rank-1 one matrices. The more general constraint is that the matrices only need to be positive-semidefinite, but trying this based

on references [121] and [123] I find it difficult to implement.

Entanglement test 2
A literature search revealed the paper "Optimal entanglement witnesses for continuous-variable systems" by Hyllus and Eisert [124]. They even provide two numerical routines that test for full inseparability and GME, respectively. These routines optimize an entanglement witness Z where $\mathrm{Tr}\left[ZV\right] - 1 < 0$ indicates entanglement. Unlike the previous method, this uses the whole covariance matrix. It also uses convex optimization[4], which is *guaranteed* to reach the optimal solution [125]. Using this method, I verify that we have full inseparability but not GME with experimental covariance matrices[5]. However, theoretical covariance matrices show GME, so why do we not we see it in the experiment? The answer is likely noise. We simulate this by mixing the theoretical ideal state with vacuum, and find the results shown in Fig. 3.8. Full inseparability can be observed (the witness is less than zero) all the way until the state is fully replaced by vacuum, while GME is much more sensitive. This agrees with literature, as it has been found that GME is more sensitive to experimental imperfections such as noise and losses compared to measurement of other types of entanglement [126, 127].

[4]Convex optimization will also be utilized in Section 3.2.
[5]This method does however not take measurement uncertainties into account.

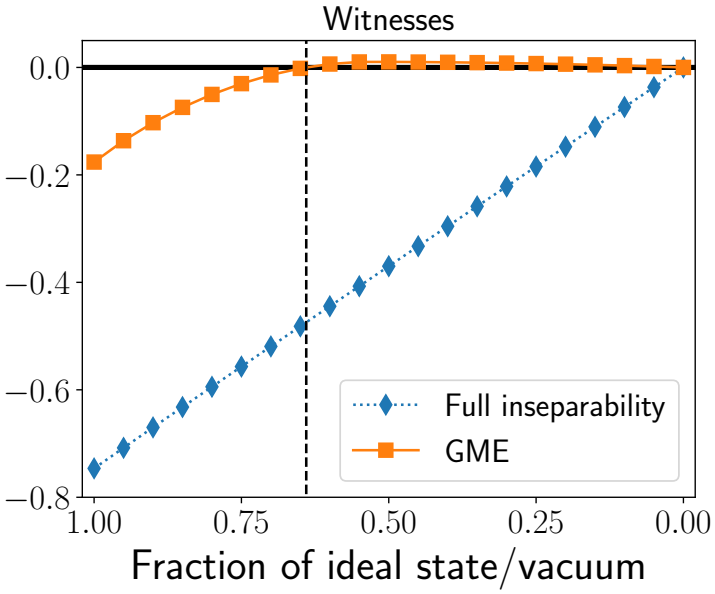

Figure 3.8: Values below zero indicates entanglement. The dashed vertical line marks the noise level where GME disappears. This value corresponds to a state purity of 0.31, which is higher that the purity of measured states. As such, it makes sense that our tests do not detect GME due to noise.

3.2 Single-mode quantum state tomography

Quantum tomography is the procedure to determine the quantum state of a physical system. It involves measuring a number of different observables and then using some computational algorithm to reconstruct the state based on the measurement results. Having an effective and robust method of quantum state reconstruction is of crucial importance in the development of quantum technology in several ways: for the verification of state preparation, the analysis of quantum dynamics and decoherence, and for retrieving information encoded in quantum states. In Paper G, I present a method of single-mode CV state tomography using convex optimization.

3.2.1 Background

Quantum state tomography methods have been developed since the early nineties when the first method was developed [128, 129]. It reconstructs the Wigner function using the fact that it is the inverse Radon transform[6] of quadrature distributions that can be measured with homodyne detection. While calculating probability distributions for observables given a known quantum state is straightforward, this *inverse problem* [131] of calculating a quantum state given measured probability distributions is fraught with issues due to the problem being *ill-posed* [132], which means the solution does not depend continuously on the data, i.e. even small variations or noise can drastically change the result, or the problem may have more than one solution. Inversion of the Radon transform is an ill-posed inverse problem, rendering it numerically unstable to calculate. There are established methods to mitigate this; for example, originally in Ref. [129] they used a filtered back-projection algorithm used in classical tomography [133]. However, a problem with this type of standard approach is that it can produce density matrices that are unphysical since quantum physical constraints are not taken into account [134]. These constraints will be stated below in Section 3.2.2.

A method that guarantees physicality of the density matrix is Maximum Likelihood estimation (MLE) which was mentioned in Section 2.2.1. An iterative MLE algorithm was introduced in the 2000s [135], and it has remained popular over time while different variations have been developed [136–139]. Currently, more advanced methods are emerging. Bayesian methods have been proposed [140–142], and neural networks for CV state tomography have started to appear [143–146]. There are downsides to all above mentioned methods: Bayesian methods require the use of Monte Carlo sampling algorithms, iterations of an MLE algorithm have to be terminated at some arbitrary point, and

[6]The Radon transform was published in 1917 and laid the foundation for conventional tomography, as it transforms a density to a set of straight line integrals, which models the signals from a CT scan. The inverted transform then gives the density [130].

neural networks are practically black boxes where the result can strongly depend on the chosen cost function.

I provide a method for state reconstruction that is both conceptually and practically simple, based on convex optimization. Convex optimization comprise a special class of mathematical optimization problems that can be numerically solved reliably and efficiently [125].

3.2.2 Tomography with convex optimization

The tomography problem can be expressed as a linear equation

$$A\vec{\rho} = \vec{b}, \tag{3.5}$$

where the vectorized density matrix $\vec{\rho}$ is the unknown variable to be solved for. The vector $\vec{b}$ contains measurement results, and the matrix A contains information on the chosen basis and measurements (see Paper F for details). Linear inversion of Eq. (3.5) to obtain the vectorized density matrix is not practical due to the ill-posedness of the problem; not only can the matrix A be very ill-conditioned, physicality of the state cannot be guaranteed so even the smallest amount of noise in the measurement data $\vec{b}$ can result in an unphysical density matrix [147]. The constraints that a physical density matrix must obey are (i) it is Hermitian, meaning its eigenvalues are real, (ii) it is positive-semidefinite, meaning no eigenvalues are less than zero, and (iii) it has trace one, meaning probabilities add up to one. These constraints can be conveniently included in a convex optimization problem:

$$\min_{\rho} \|A\vec{\rho} - \vec{b}\|_2^2, \tag{3.6}$$

$$\text{subject to } \rho \succeq 0, \tag{3.7}$$

$$\operatorname{Tr}\rho = 1. \tag{3.8}$$

We minimize the convex cost function[7] (3.6) over the set of density matrices, which is a convex set [148] (illustrated in Fig. 3.9). Convex optimization problems are easier to solve than general nonlinear optimization problems, but most importantly, it can be shown that every local minimum to a convex optimization problem is also a global minimum, guaranteeing an optimal solution [125]. There are efficient numerical methods that solve this type of problems, and software packages that provide them. I used the open source Python package CVXPY [149–151]. Being able to utilize already existing software makes this state reconstruction procedure very easy to implement. After loading measurement data into the array $\vec{b}$ and constructing the matrix A, the short code in block 3.10 is all that is needed.

Realistically, there is noise in measurements. The method can compensate for this if the noise level is known. For example, we can test the method with experimental data from Paper C. Fig. 3.11(a) shows a histogram of the mea-

[7] This corresponds to the least-squares solution to the linear equation (3.5).

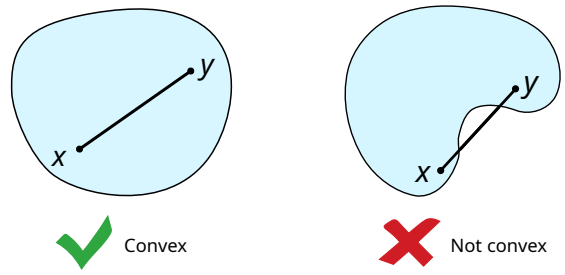

Figure 3.9: A set is convex if all its other points are "visible" from a point anywhere within it.

```
import cvxpy as cp

# Initialize the unknown variable X as an N x N Hermitian matrix.
X = cp.Variable((N,N), hermitian=True)

# Define the cost function as the 2-norm of AX_vec-b.
cost = cp.norm(A @ cp.vec(X) - b, 2)

# Set the two constraints.
constraints = [cp.trace(X) == 1, X >> 0 ]

# Set up and solve the problem!
prob = cp.Problem(cp.Minimize(cost), constraints)
prob.solve();

# Get the density matrix.
rho = X.value
```

Code block 3.10: Only a few lines of code is needed to implement the convex tomography procedure. Compare with Eqs. (3.6)–(3.8).

surement data when the signal we actually want to measure is on. Fig. 3.11(b) shows the measurement data when the signal is off, meaning only noise is captured. These two cases are practically impossible to distinguish by eye, but Fig. 3.11(c) shows the 'Signal Off' histogram subtracted from the 'Signal On' histogram so it can be seen that there is a slight difference. Taking a slice from the 'Off' histogram as indicated by the dashed orange line in Fig. 3.11(b), we see in Fig. 3.11(d) that it matches a thermal state with 4.8 photons on average. The Wigner function of the reconstructed state is shown in the top left of Fig. 3.12. The bottom row of the figure shows the result from a maximum likelihood estimation [152] that was used for Paper C. The results agree, which is good. However, the used maximum likelihood method uses the measurement histograms to calculate moments of the field for both 'Off' and 'On' data, which are in turn used for state estimation. This necessitates a truncation of the Hilbert space to a small size, since using a larger space requires higher and higher-order moments, and there is more measurement uncertainty

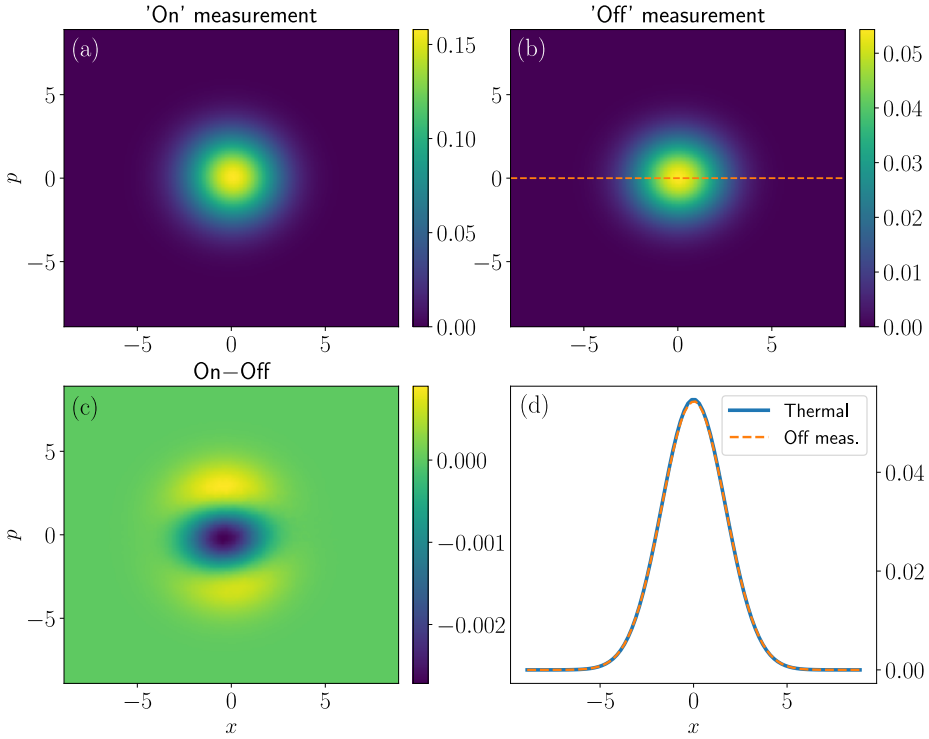

Figure 3.11: (a) Normalized histogram of measurement data with the signal on. (b) Normalized histogram of measurement data with the signal off. The dashed orange line indicates where the amplitude is plotted in (d). (c) The subtraction of histograms to visualize the small difference between them. (c) The dashed orange line is the line cut indicated in (b). The blue line is the corresponding curve for an ideal thermal state with an average of 4.8 photons.

for higher moments. After determining the number of noise photons from the 'Off' histogram [cf. Fig. 3.11(d)], the convex optimization uses the 'On' histogram directly and faces no such issues.

We can also apply the convex optimization state reconstruction to the Wigner function measurements in Paper D. For example, with the measurement data in Fig. 2.12(b) we obtain the result shown in the top row of Fig. 3.13. For the paper, a neural network-based method [145, 146] was used and its outcome can be seen in the bottom row of the figure. The results agree quite well. All in all, the convex optimization tomography method works at least as well as other methods.

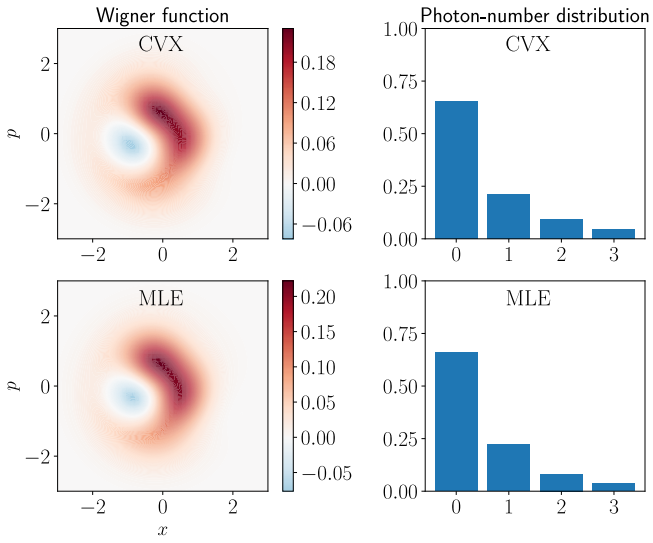

Figure 3.12: Comparison between maximum likelihood estimation (MLE) [152] and convex optimization (CVX) reconstruction using the data in Fig. 3.11. The resulting states are virtually identical with 0.99 fidelity.

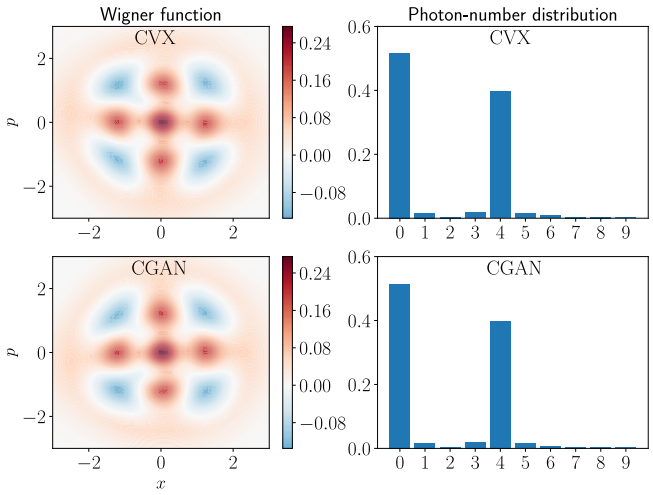

Figure 3.13: Comparison between reconstructions from a type of neural network, specifically a conditional generative adversarial network (CGAN) [145, 146] and convex optimization (CVX) using the data in Fig. 2.12(b). The resulting states are similar, with fidelity 0.95 both with respect to each other and the ideal state.

Chapter 4

Conclusions

4.1 Summary

In the last decade, there has been tremendous progress in the ability to experimentally study and even control quantum systems on the nanoscale. This has lead to rapid advancements in quantum technology with applications in secure communications, sensing, and computing, where it can have advantages over classical technology. This thesis was mainly focused on enabling quantum computing, and described a variety of projects that can collectively be described as generation and characterization of microwave quantum states of light that could be useful for this purpose.

To begin with, Chapter 1 provided a brief overview of the quantized electromagnetic field, and then introduced a property called Wigner-negativity that quantum states of light may possess. This is important because all quantum states are not equally useful for quantum computing, and Wigner-negative states are a prerequisite for a quantum computer to gain an exponential speedup compared to an ordinary computer. This introductory chapter also described how superconducting circuits which operate at frequencies in the microwave domain are advantageous for creating such states.

Chapter 2 was about generation of Wigner-negative quantum states, and described Papers A-E. In Paper A we showed by numerical simulation that the simplest quantum model of light-matter interaction, a two-level atom coupled to a monochromatic electromagnetic field, can produce propagating quantum fields of light that are Wigner-negative. Paper B was a continuation of the first paper, where the model was extended to include realistic imperfections if the two-level atom is realized by a transmon qubit, which is an implementation of a quantum bit in superconducting circuits. Since Wigner-negativity was still present, the system was implemented and verified experimentally in Paper C. A similar idea but with a nonlinear cavity instead of a two-level atom was theoretically and

numerically explored in Paper D. In Paper E, we generated microwave states that can be utilized for quantum error correcting codes in a three-dimensional cavity.

The next part of the thesis, Chapter 3, was focused on quantum state characterization. When trying to generate a certain quantum state with certain properties, it is important to verify what state was actually prepared. First was Paper F, which was actually not about Wigner-negative states, but instead entangled states. Determining the form of entanglement between more than two quantum states can be a complicated task, and that was done in this paper. Finally, Paper G introduced a simple method to obtain the full density matrix from different types of measurement data. The method is based on convex optimization, which means it is guaranteed to reach the optimal solution, unlike other popular methods.

4.2 Outlook

Propagating states can be used for information processing and communication tasks since they are able to relay quantum information between nodes of a modular distributed quantum system. We do not yet know exactly if, or how, our propagating states in Section 2.2 can be utilized for quantum computing, but one possibility is that they could be used to distill other resourceful states that are known to be useful, for example the cubic phase state [20, 153]. The question of why a Gaussian temporal mode shape seems to maximize Wigner-negativity is also as of now unanswered.

Quantum states are inherently fragile—inevitable interactions with the environment destroys quantum coherence (i.e. "quantumness") after a short time. For this reason, quantum error correction is thought to be a requirement in order to perform useful quantum algorithms that surpass the capabilities of classical computers. One of the leading approaches to error correction is to encode qubits in bosonic states inside 3D cavities, such as those prepared in Section 2.3. A natural next step would be to implement an error-correcting procedure. One appealing approach is *autonomous* error correction that does not require feedback and adaptive control. It does, however, need multiple microwave drive tones to address transitions between different energy levels simultaneously. Our experimental setup is capable of providing this, but it turns out that multiple cavity drives shift the auxiliary qubit's energy in a nonlinear fashion even at fairly weak drive strengths. This was not anticipated, and needs to be further investigated.

The same type of microwave platform [154] as mentioned above was used for the entanglement experiment in Section 3.1 where two drives were used to create multimode entanglement, but we could not identify any cluster state. Since the drives determine the entanglement between different frequency modes, more drives could be added to create different entanglement structures. We are working on optimizing drive frequencies given a particular target cluster state. This

would also produce a Gaussian state, which could be used for universal quantum computing only if a non-Gaussian operation such as the cubic phase gate could be performed. It would also be interesting to investigate the properties of a non-Gaussian cluster. This has been done in quantum optics, where they consider the effects of photon subtraction or addition which are non-Gaussian operations. This requires single-photon detection which is not currently viable for circuit-QED, but what would happen if a propagating state such as those described in Section 2.2 were used as input instead, for example? Additionally, there is also the application of Gaussian entangled states for reservoir computing [155], which is a type of machine learning framework. Machine learning is one area where quantum effects can possibly boost performance [156].

The quantum state tomography in Section 3.2 can take noise into account if the noise level is specified, but measurement uncertainties that are unaccounted for will introduce slight errors in the state reconstruction. Determining the magnitude of these errors is a nontrivial endeavor for any method, but should be researched since it is of high importance. It is also of interest to investigate which measurements should be made to achieve the highest accuracy, and how many are needed. This has been researched for qubit-based systems, but less so for continuous-variables. Fewer measurements would be beneficial, since state tomography can be very time consuming.

All in all, there are several intriguing avenues to continue to explore for all of these projects.

Bibliography

[1] *The Physics of Quantum Information* (Springer, Berlin, Germany, 2000).

[2] C. J. Hoofnagle and S. L. Garfinkel, in *Quantum Sensing and Metrology* (Cambridge University Press, 2022) pp. 31–76.

[3] *Applied Quantum Cryptography* (Springer, Berlin, Germany, 2010).

[4] M. A. Nielsen and I. L. Chuang, *Quantum Computation and Quantum Information* (Cambridge University Press, Cambridge, England, 2010).

[5] S. Lloyd and S. L. Braunstein, "Quantum Computation over Continuous Variables", Phys. Rev. Lett. **82**, 1784–1787 (1999).

[6] S. L. Braunstein and P. van Loock, "Quantum information with continuous variables", Rev. Mod. Phys. **77**, 513–577 (2005).

[7] M. J. Clerk, "VIII. A dynamical theory of the electromagnetic field", Philos. Trans. R. Soc. Lond. **155**, 459–512 (1865).

[8] C. Fabre and N. Treps, "Modes and states in quantum optics", Rev. Mod. Phys. **92**, 035005 (2020).

[9] R. Loudon, *The Quantum Theory of Light*, 3rd ed. (Oxford University Press, 2000).

[10] R. R. Puri, in *Mathematical Methods of Quantum Optics* (Springer, Berlin, Germany, 2001) pp. 119–136.

[11] U. Leonhardt and H. Paul, "Measuring the quantum state of light", Prog. Quantum Electron. **19**, 89–130 (1995).

[12] D. F. Vanderwerf, *The story of light science*, 1st ed. (Springer International Publishing, 2017).

[13] W. T. Coffey, "A Concise Treatise on Quantum Mechanics in Phase Space", Contemp. Phys. **56**, 85–87 (2015).

[14] W. P. Schleich, *Quantum Optics in Phase Space* (Wiley-VCH Verlag, 2001).

[15] P. Bertet, A. Auffeves, P. Maioli, S. Osnaghi, T. Meunier, M. Brune, J. M. Raimond, and S. Haroche, "Direct Measurement of the Wigner Function of a One-Photon Fock State in a Cavity", Phys. Rev. Lett. **89**, 200402 (2002).

[16] L. G. Lutterbach and L. Davidovich, "Method for Direct Measurement of the Wigner Function in Cavity QED and Ion Traps", Phys. Rev. Lett. **78**, 2547–2550 (1997).

[17] K. Banaszek, C. Radzewicz, K. Wódkiewicz, and J. S. Krasiński, "Direct measurement of the Wigner function by photon counting", Phys. Rev. A **60**, 674–677 (1999).

[18] V. Veitch, N. Wiebe, C. Ferrie, and J. Emerson, "Efficient simulation scheme for a class of quantum optics experiments with non-negative Wigner representation", New J. Phys. **15**, 013037 (2013).

[19] A. Mari and J. Eisert, "Positive Wigner Functions Render Classical Simulation of Quantum Computation Efficient", Phys. Rev. Lett. **109**, 230503 (2012).

[20] V. Veitch, C. Ferrie, D. Gross, and J. Emerson, "Negative quasi-probability as a resource for quantum computation", New J. Phys. **14**, 113011 (2012).

[21] S. Rahimi-Keshari, T. C. Ralph, and C. M. Caves, "Sufficient Conditions for Efficient Classical Simulation of Quantum Optics", Phys. Rev. X **6**, 021039 (2016).

[22] A. Barenco, C. H. Bennett, R. Cleve, D. P. DiVincenzo, N. Margolus, P. Shor, T. Sleator, J. A. Smolin, and H. Weinfurter, "Elementary gates for quantum computation", Phys. Rev. A **52**, 3457–3467 (1995).

[23] S. Bravyi and A. Kitaev, "Universal quantum computation with ideal Clifford gates and noisy ancillas", Phys. Rev. A **71**, 022316 (2005).

[24] S. Aaronson and D. Gottesman, "Improved simulation of stabilizer circuits", Phys. Rev. A **70**, 052328 (2004).

[25] K. Życzkowski and I. Bengtsson, "On Duality between Quantum Maps and Quantum States", Open Syst. Inf. Dyn. **11**, 3–42 (2004).

[26] M. Jiang, S. Luo, and S. Fu, "Channel-state duality", Phys. Rev. A **87**, 022310 (2013).

[27] R. L. Hudson, "When is the wigner quasi-probability density non-negative?", Rep. Math. Phys. **6**, 249–252 (1974).

[28] G. Wendin and V. S. Shumeiko, "Quantum bits with Josephson junctions (Review Article)", Low Temp. Phys. **33**, 724–744 (2007).

[29] J. M. Martinis and K. Osborne, "Superconducting Qubits and the Physics of Josephson Junctions: Les Houches conference proceedings", arXiv 10.48550/arXiv.cond-mat/0402415 (2004), cond-mat/0402415 .

[30] D. Stornaiuolo and F. Tafuri, in *Fundamentals and Frontiers of the Josephson Effect* (Springer, Cham, Switzerland, 2019) pp. 275–337.

[31] D. A. Wells, "Application of the Lagrangian Equations to Electrical Circuits", J. Appl. Phys. **9**, 312–320 (1938).

[32] A. Blais, A. L. Grimsmo, S. M. Girvin, and A. Wallraff, "Circuit quantum electrodynamics", Rev. Mod. Phys. **93**, 025005 (2021).

[33] P. Krantz, M. Kjaergaard, F. Yan, T. P. Orlando, S. Gustavsson, and W. D. Oliver, "A quantum engineer's guide to superconducting qubits", Appl. Phys. Rev. **6**, 021318 (2019).

[34] V. V. Sivak, N. E. Frattini, V. R. Joshi, A. Lingenfelter, S. Shankar, and M. H. Devoret, "Kerr-Free Three-Wave Mixing in Superconducting Quantum Circuits", Phys. Rev. Appl. **11**, 054060 (2019).

[35] B. Abdo, A. Kamal, and M. Devoret, "Nondegenerate three-wave mixing with the Josephson ring modulator", Phys. Rev. B **87**, 014508 (2013).

[36] *SQUID Sensors* (Springer Netherlands, 1996).

[37] T. Orlando and K. Delin, *Foundations of Applied Superconductivity*, Electrical Engineering Series (Addison-Wesley, 1991).

[38] S. E. Rasmussen, K. S. Christensen, S. P. Pedersen, L. B. Kristensen, T. Bækkegaard, N. J. S. Loft, and N. T. Zinner, "Superconducting Circuit Companion—an Introduction with Worked Examples", PRX Quantum **2**, 040204 (2021).

[39] D. Tucker, *Circuits with Periodically-varying Parameters: Including Modulators and Parametric Amplifiers*, Trends and developments in engineering series (Van Nostrand, 1964).

[40] M. Göppl, A. Fragner, M. Baur, R. Bianchetti, S. Filipp, J. M. Fink, P. J. Leek, G. Puebla, L. Steffen, and A. Wallraff, "Coplanar waveguide resonators for circuit quantum electrodynamics", J. Appl. Phys. **104**, 113904 (2008).

[41] D. Roy, C. M. Wilson, and O. Firstenberg, "Colloquium: Strongly interacting photons in one-dimensional continuum", Rev. Mod. Phys. **89**, 021001 (2017).

[42] M. Reagor, H. Paik, G. Catelani, L. Sun, C. Axline, E. Holland, I. M. Pop, N. A. Masluk, T. Brecht, L. Frunzio, M. H. Devoret, L. Glazman, and R. J. Schoelkopf, "Reaching 10 ms single photon lifetimes for superconducting aluminum cavities", Appl. Phys. Lett. **102**, 192604 (2013).

[43] G. S. Buller and R. J. Collins, "Single-photon generation and detection", Meas. Sci. Technol. **21**, 012002 (2009).

[44] M. D. Eisaman, J. Fan, A. Migdall, and S. V. Polyakov, "Invited Review Article: Single-photon sources and detectors", Rev. Sci. Instrum. **82**, 071101 (2011).

[45] K. Inomata, Z. Lin, K. Koshino, W. D. Oliver, J.-S. Tsai, T. Yamamoto, and Y. Nakamura, "Single microwave-photon detector using an artificial Λ-type three-level system", Nat. Commun. **7**, 1–7 (2016).

[46] R. Lescanne, S. Deléglise, E. Albertinale, U. Réglade, T. Capelle, E. Ivanov, T. Jacqmin, Z. Leghtas, and E. Flurin, "Irreversible Qubit-Photon Coupling for the Detection of Itinerant Microwave Photons", Phys. Rev. X **10**, 021038 (2020).

[47] H. Breuer, P. Breuer, F. Petruccione, and S. Petruccione, *The Theory of Open Quantum Systems* (Oxford University Press, 2002).

[48] K. J. Blow, R. Loudon, S. J. D. Phoenix, and T. J. Shepherd, "Continuum fields in quantum optics", Phys. Rev. A **42**, 4102–4114 (1990).

[49] B. Brecht, D. V. Reddy, C. Silberhorn, and M. G. Raymer, "Photon Temporal Modes: A Complete Framework for Quantum Information Science", Phys. Rev. X **5**, 041017 (2015).

[50] B. R. Mollow, "Power Spectrum of Light Scattered by Two-Level Systems", Phys. Rev. **188**, 1969–1975 (1969).

[51] H. J. Kimble and L. Mandel, "Theory of resonance fluorescence", Phys. Rev. A **13**, 2123–2144 (1976).

[52] H. J. Kimble, M. Dagenais, and L. Mandel, "Photon Antibunching in Resonance Fluorescence", Phys. Rev. Lett. **39**, 691–695 (1977).

[53] R. Loudon, "Squeezing in resonance fluorescence", Opt. Commun. **49**, 24–28 (1984).

[54] C. H. H. Schulte, J. Hansom, A. E. Jones, C. Matthiesen, C. Le Gall, and M. Atatüre, "Quadrature squeezed photons from a two-level system", Nature **525**, 222 (2015).

[55] H. M. Wiseman and G. J. Milburn, *Quantum Measurement and Control* (Cambridge University Press, Cambridge, England, UK, 2009).

[56] P. Kloeden and E. Platen, *Numerical Solution of Stochastic Differential Equations*, Stochastic Modelling and Applied Probability (Springer Berlin Heidelberg, 2011).

[57] R. J. Rossi, *Mathematical Statistics: An Introduction to Likelihood Based Inference* (Wiley, Hoboken, NJ, USA, 2018).

[58] M. G. A. Paris, G. M. D'Ariano, and M. F. Sacchi, "Maximum-likelihood method in quantum estimation", AIP Conf. Proc. **568**, 456–467 (2001).

[59] J. Sakurai and J. Napolitano, *Modern Quantum Mechanics* (Addison-Wesley, 2011).

[60] M. J. Collett and C. W. Gardiner, "Squeezing of intracavity and travelling-wave light fields produced in parametric amplification", Phys. Rev. A **30**, 1386–1391 (1984).

[61] S. Puri, S. Boutin, and A. Blais, "Engineering the quantum states of light in a Kerr-nonlinear resonator by two-photon driving", npj Quantum Inf. **3**, 1–7 (2017).

[62] R. Y. Teh, F.-X. Sun, R. E. S. Polkinghorne, Q. Y. He, Q. Gong, P. D. Drummond, and M. D. Reid, "Dynamics of transient cat states in degenerate parametric oscillation with and without nonlinear Kerr interactions", Phys. Rev. A **101**, 043807 (2020).

[63] F.-X. Sun, Q. He, Q. Gong, R. Y. Teh, M. D. Reid, and P. D. Drummond, "Schr\"odinger cat states and steady states in subharmonic generation with Kerr nonlinearities", Phys. Rev. A **100**, 033827 (2019).

[64] K. V. Kheruntsyan, D. S. Krähmer, G. Y. Kryuchkyan, and K. G. Petrossian, "Wigner function for a generalized model of a parametric oscillator: phase-space tristability, competition and nonclassical effects", Opt. Commun. **139**, 157–164 (1997).

[65] A. H. Kiilerich and K. Mølmer, "Input-Output Theory with Quantum Pulses", Phys. Rev. Lett. **123**, 123604 (2019).

[66] J. R. Johansson, P. D. Nation, and F. Nori, "QuTiP 2: A Python framework for the dynamics of open quantum systems", Comput. Phys. Commun. **184**, 1234–1240 (2013), `https://qutip.org/`.

[67] F. Albarelli, M. G. Genoni, M. G. A. Paris, and A. Ferraro, "Resource theory of quantum non-Gaussianity and Wigner negativity", Phys. Rev. A **98**, 052350 (2018).

[68] P. Virtanen, R. Gommers, T. E. Oliphant, M. Haberland, T. Reddy, D. Cournapeau, E. Burovski, P. Peterson, W. Weckesser, J. Bright, S. J. van der Walt, M. Brett, J. Wilson, K. J. Millman, N. Mayorov, A. R. J. Nelson, E. Jones, R. Kern, E. Larson, C. J. Carey, İ. Polat, Y. Feng, E. W.

Moore, J. VanderPlas, D. Laxalde, J. Perktold, R. Cimrman, I. Henriksen, E. A. Quintero, C. R. Harris, A. M. Archibald, A. H. Ribeiro, F. Pedregosa, P. van Mulbregt, and SciPy 1.0 Contributors, "SciPy 1.0: Fundamental Algorithms for Scientific Computing in Python", Nature Methods **17**, 261–272 (2020).

[69] J. Roffe, "Quantum error correction: an introductory guide", Contemp. Phys. **60**, 226–245 (2019).

[70] M. H. Michael, M. Silveri, R. T. Brierley, V. V. Albert, J. Salmilehto, L. Jiang, and S. M. Girvin, "New Class of Quantum Error-Correcting Codes for a Bosonic Mode", Phys. Rev. X **6**, 031006 (2016).

[71] S. M. Girvin, "Schrodinger Cat States in Circuit QED", arXiv 10.48550/arXiv.1710.03179 (2017), 1710.03179 .

[72] D. Gottesman, A. Kitaev, and J. Preskill, "Encoding a qubit in an oscillator", Phys. Rev. A **64**, 012310 (2001).

[73] D. F. Walls and G. J. Milburn, *Quantum Optics*, Springer Study Edition (Springer, 1995).

[74] D. I. Schuster, A. A. Houck, J. A. Schreier, A. Wallraff, J. M. Gambetta, A. Blais, L. Frunzio, J. Majer, B. Johnson, M. H. Devoret, S. M. Girvin, and R. J. Schoelkopf, "Resolving photon number states in a superconducting circuit", Nature **445**, 515–518 (2007).

[75] R. W. Heeres, B. Vlastakis, E. Holland, S. Krastanov, V. V. Albert, L. Frunzio, L. Jiang, and R. J. Schoelkopf, "Cavity State Manipulation Using Photon-Number Selective Phase Gates", Phys. Rev. Lett. **115**, 137002 (2015).

[76] S. Krastanov, V. V. Albert, C. Shen, C.-L. Zou, R. W. Heeres, B. Vlastakis, R. J. Schoelkopf, and L. Jiang, "Universal control of an oscillator with dispersive coupling to a qubit", Phys. Rev. A **92**, 040303 (2015).

[77] R. Vinter, *Optimal Control* (Birkhäuser, Boston, MA, USA, 2010).

[78] J. Werschnik and E. K. U. Gross, "Quantum optimal control theory", J. Phys. B: At. Mol. Opt. Phys. **40**, R175-R211 (2007).

[79] S. Grivopoulos, *Optimal Control of Quantum Systems*, Ph.D. thesis, University of California, Santa Barbara (2005).

[80] D. L. Hocker, *Lessons from the quantum control landscape: Robust optimal control of quantum systems and optimal control of nonlinear Schrödinger equations*, Ph.D. thesis, Princeton University (2016).

[81] R. Huneault, *Time-Optimal Control of Closed Quantum Systems*, Ph.D. thesis, University of Waterloo (2009).

[82] R. M. Fisher, *Optimal control of multi-level quantum systems*, Ph.D. thesis, Technical University of Munichen (2010).

[83] D. L. Goodwin, *Advanced Optimal Control Methods for Spin Systems*, Ph.D. thesis, University of Southampton (2017).

[84] Q. Ansel, *Optimal control of inhomogeneous spin ensembles : applications in NMR and quantum optics*, Ph.D. thesis, Technical University of Munich (2018).

[85] D. J. Egger, *Optimal Control and Quantum Simulations in Superconducting Quantum Devices*, Ph.D. thesis, Saarland University (2014).

[86] "Q-CTRL documentation, Boulder Opal application notes: Designing fast optimal SNAP gates in superconducting resonators", [Online; accessed 8. Jul. 2022] (2022).

[87] Y. Zheng, O. Hahn, P. Stadler, P. Holmvall, F. Quijandría, A. Ferraro, and G. Ferrini, "Gaussian Conversion Protocols for Cubic Phase State Generation", PRX Quantum **2**, 010327 (2021).

[88] Q. Wang, Y. Tian, W. Li, L. Tian, Y. Wang, and Y. Zheng, "High-fidelity quantum teleportation toward cubic phase gates beyond the no-cloning limit", Phys. Rev. A **103**, 062421 (2021).

[89] D. Chruściński and G. Sarbicki, "Entanglement witnesses: construction, analysis and classification", J. Phys. A: Math. Theor. **47**, 483001 (2014).

[90] C. H. Bennett, G. Brassard, C. Crépeau, R. Jozsa, A. Peres, and W. K. Wootters, "Teleporting an unknown quantum state via dual classical and Einstein-Podolsky-Rosen channels", Phys. Rev. Lett. **70**, 1895–1899 (1993).

[91] J. Yin, Y.-H. Li, S.-K. Liao, M. Yang, Y. Cao, L. Zhang, J.-G. Ren, W.-Q. Cai, W.-Y. Liu, S.-L. Li, R. Shu, Y.-M. Huang, L. Deng, L. Li, Q. Zhang, N.-L. Liu, Y.-A. Chen, C.-Y. Lu, X.-B. Wang, F. Xu, J.-Y. Wang, C.-Z. Peng, A. K. Ekert, and J.-W. Pan, "Entanglement-based secure quantum cryptography over 1,120 kilometres", Nature **582**, 501–505 (2020).

[92] D. Markham and B. C. Sanders, "Graph states for quantum secret sharing", Phys. Rev. A **78**, 042309 (2008).

[93] N. Shettell and D. Markham, "Graph States as a Resource for Quantum Metrology", Phys. Rev. Lett. **124**, 110502 (2020).

[94] Y. Wang and K. Fang, "Continuous-variable graph states for quantum metrology", Phys. Rev. A **102**, 052601 (2020).

[95] N. Zou, "Quantum Entanglement and Its Application in Quantum Communication", J. Phys. Conf. Ser. **1827**, 012120 (2021).

[96] R. Raussendorf and H. J. Briegel, "A One-Way Quantum Computer", Phys. Rev. Lett. **86**, 5188–5191 (2001).

[97] R. Raussendorf, D. E. Browne, and H. J. Briegel, "Measurement-based quantum computation on cluster states", Phys. Rev. A **68**, 022312 (2003).

[98] S. Takeda, K. Takase, and A. Furusawa, "On-demand photonic entanglement synthesizer", Sci. Adv. **5**, eaaw4530 (2019).

[99] N. C. Menicucci, P. van Loock, M. Gu, C. Weedbrook, T. C. Ralph, and M. A. Nielsen, "Universal Quantum Computation with Continuous-Variable Cluster States", Phys. Rev. Lett. **97**, 110501 (2006).

[100] M. Gu, C. Weedbrook, N. C. Menicucci, T. C. Ralph, and P. van Loock, "Quantum computing with continuous-variable clusters", Phys. Rev. A **79**, 062318 (2009).

[101] S. Yokoyama, R. Ukai, S. C. Armstrong, C. Sornphiphatphong, T. Kaji, S. Suzuki, J.-i. Yoshikawa, H. Yonezawa, N. C. Menicucci, and A. Furusawa, "Ultra-large-scale continuous-variable cluster states multiplexed in the time domain", Nat. Photonics **7**, 982–986 (2013).

[102] J.-i. Yoshikawa, S. Yokoyama, T. Kaji, C. Sornphiphatphong, Y. Shiozawa, K. Makino, and A. Furusawa, "Invited Article: Generation of one-million-mode continuous-variable cluster state by unlimited time-domain multiplexing", APL Photonics **1**, 060801 (2016).

[103] W. Asavanant, Y. Shiozawa, S. Yokoyama, B. Charoensombutamon, H. Emura, R. N. Alexander, S. Takeda, J.-i. Yoshikawa, N. C. Menicucci, H. Yonezawa, and A. Furusawa, "Generation of time-domain-multiplexed two-dimensional cluster state", Science **366**, 373–376 (2019).

[104] R. N. Alexander, P. Wang, N. Sridhar, M. Chen, O. Pfister, and N. C. Menicucci, "One-way quantum computing with arbitrarily large time-frequency continuous-variable cluster states from a single optical parametric oscillator", Phys. Rev. A **94**, 032327 (2016).

[105] M. V. Larsen, X. Guo, C. R. Breum, J. S. Neergaard-Nielsen, and U. L. Andersen, "Deterministic generation of a two-dimensional cluster state", Science **366**, 369–372 (2019).

[106] C. W. Sandbo Chang, M. Simoen, J. Aumentado, C. Sabín, P. Forn-Díaz, A. M. Vadiraj, F. Quijandría, G. Johansson, I. Fuentes, and C. M. Wilson, "Generating Multimode Entangled Microwaves with a Superconducting Parametric Cavity", Phys. Rev. Appl. **10**, 044019 (2018).

[107] X.-L. Zong, H.-H. Yin, W. Song, and Z.-L. Cao, "Monogamy of Quantum Entanglement", Front. Phys. **0**, 10.3389/fphy.2022.880560 (2022).

[108] W. Dür and J. I. Cirac, "Classification of multiqubit mixed states: Separability and distillability properties", Phys. Rev. A **61**, 042314 (2000).

[109] Y. Hong and S. Luo, "Detecting k-nonseparability via local uncertainty relations", Phys. Rev. A **93**, 042310 (2016).

[110] R. Y. Teh and M. D. Reid, "Criteria to detect genuine multipartite entanglement using spin measurements", Phys. Rev. A **100**, 022126 (2019).

[111] R. Y. Teh and M. D. Reid, "Criteria for genuine N-partite continuous-variable entanglement and Einstein-Podolsky-Rosen steering", Phys. Rev. A **90**, 062337 (2014).

[112] J. Aumentado, "Superconducting Parametric Amplifiers: The State of the Art in Josephson Parametric Amplifiers", IEEE Microwave Mag. **21**, 45–59 (2020).

[113] C. Li, *Nonlinear Optics* (Springer Nature, Singapore, 2017).

[114] K. Löcherer and C. Brandt, *Parametric Electronics: An Introduction*, Springer Series in Electronics and Photonics (Springer Berlin Heidelberg, 2013).

[115] B. W. Adams, in *Nonlinear Optics, Quantum Optics, and Ultrafast Phenomena with X-Rays: Physics with X-Ray Free-Electron Lasers* (Springer, Boston, MA, Boston, MA, USA, 2003) pp. 109–158.

[116] C. Weedbrook, S. Pirandola, R. García-Patrón, N. J. Cerf, T. C. Ralph, J. H. Shapiro, and S. Lloyd, "Gaussian quantum information", Rev. Mod. Phys. **84**, 621–669 (2012).

[117] S. Gerke, J. Sperling, W. Vogel, Y. Cai, J. Roslund, N. Treps, and C. Fabre, "Full Multipartite Entanglement of Frequency-Comb Gaussian States", Phys. Rev. Lett. **114**, 050501 (2015).

[118] A. Serafini, *Quantum Continuous Variables: A Primer of Theoretical Methods* (CRC Press, 2017).

[119] L.-M. Duan, G. Giedke, J. I. Cirac, and P. Zoller, "Inseparability Criterion for Continuous Variable Systems", Phys. Rev. Lett. **84**, 2722–2725 (2000).

[120] M. Lewenstein, B. Kraus, J. I. Cirac, and P. Horodecki, "Optimization of entanglement witnesses", Phys. Rev. A **62**, 052310 (2000).

[121] E. Shchukin and P. van Loock, "Recovering Quantum Properties of Continuous-Variable States in the Presence of Measurement Errors", Phys. Rev. Lett. **117**, 140504 (2016).

[122] L. K. Shalm, D. R. Hamel, Z. Yan, C. Simon, K. J. Resch, and T. Jennewein, "Three-photon energy–time entanglement - Nature Physics", Nat. Phys. **9**, 19–22 (2013).

[123] E. Shchukin and P. van Loock, "Generalized conditions for genuine multipartite continuous-variable entanglement", Phys. Rev. A **92**, 042328 (2015).

[124] P. Hyllus and J. Eisert, "Optimal entanglement witnesses for continuous-variable systems", New J. Phys. **8**, 51 (2006).

[125] S. Boyd and L. Vandenberghe, *Convex Optimization* (Cambridge University Press, Cambridge, England, UK, 2004).

[126] O. Gühne and G. Tóth, "Entanglement detection", Phys. Rep. **474**, 1–75 (2009).

[127] T. Aoki, N. Takei, H. Yonezawa, K. Wakui, T. Hiraoka, A. Furusawa, and P. van Loock, "Experimental Creation of a Fully Inseparable Tripartite Continuous-Variable State", Phys. Rev. Lett. **91**, 080404 (2003).

[128] K. Vogel and H. Risken, "Determination of quasiprobability distributions in terms of probability distributions for the rotated quadrature phase", Phys. Rev. A **40**, 2847–2849(R) (1989).

[129] D. T. Smithey, M. Beck, M. G. Raymer, and A. Faridani, "Measurement of the Wigner distribution and the density matrix of a light mode using optical homodyne tomography: Application to squeezed states and the vacuum", Phys. Rev. Lett. **70**, 1244–1247 (1993).

[130] O. Taubmann, M. Berger, M. Bögel, Y. Xia, M. Balda, and A. Maier, in *Medical Imaging Systems: An Introductory Guide* (Springer, Cham, Switzerland, 2018) pp. 147–189.

[131] A. Kirsch, *An Introduction to the Mathematical Theory of Inverse Problems* (Springer, New York, NY, USA, 2011).

[132] S. I. Kabanikhin, *Inverse and ill-posed problems* (De Gruyter, Berlin, Germany, 2011).

[133] G. T. Herman, *Fundamentals of Computerized Tomography* (Springer, London, England, UK, 2009).

[134] A. I. Lvovsky and M. G. Raymer, "Continuous-variable optical quantum-state tomography", Rev. Mod. Phys. **81**, 299–332 (2009).

[135] A. I. Lvovsky, "Iterative maximum-likelihood reconstruction in quantum homodyne tomography", J. Opt. B: Quantum Semiclassical Opt. **6**, S556-S559 (2004).

[136] J. Řeháček, Z. Hradil, E. Knill, and A. I. Lvovsky, "Diluted maximum-likelihood algorithm for quantum tomography", Phys. Rev. A **75**, 042108 (2007).

[137] J. Shang, Z. Zhang, and H. K. Ng, "Superfast maximum-likelihood reconstruction for quantum tomography", Phys. Rev. A **95**, 062336 (2017).

[138] R. Blume-Kohout, "Hedged Maximum Likelihood Quantum State Estimation", Phys. Rev. Lett. **105**, 200504 (2010).

[139] T. Baumgratz, A. Nüßeler, M. Cramer, and M. B. Plenio, "A scalable maximum likelihood method for quantum state tomography", New J. Phys. **15**, 125004 (2013).

[140] R. Blume-Kohout, "Optimal, reliable estimation of quantum states", New J. Phys. **12**, 043034 (2010).

[141] C. Granade, J. Combes, and D. G. Cory, "Practical Bayesian tomography", New J. Phys. **18**, 033024 (2016).

[142] J. M. Lukens, K. J. H. Law, A. Jasra, and P. Lougovski, "A practical and efficient approach for Bayesian quantum state estimation", New J. Phys. **22**, 063038 (2020).

[143] E. S. Tiunov, V. V. Tiunova (Vyborova), A. E. Ulanov, A. I. Lvovsky, and A. K. Fedorov, "Experimental quantum homodyne tomography via machine learning", Optica **7**, 448–454 (2020).

[144] S. Ghosh, A. Opala, M. Matuszewski, T. Paterek, and T. C. H. Liew, "Reconstructing Quantum States With Quantum Reservoir Networks", IEEE Trans. Neural Networks Learn. Syst. **32**, 3148–3155 (2020).

[145] S. Ahmed, C. Sánchez Muñoz, F. Nori, and A. F. Kockum, "Quantum State Tomography with Conditional Generative Adversarial Networks", Phys. Rev. Lett. **127**, 140502 (2021).

[146] S. Ahmed, C. Sánchez Muñoz, F. Nori, and A. F. Kockum, "Classification and reconstruction of optical quantum states with deep neural networks", Phys. Rev. Res. **3**, 033278 (2021).

[147] D. Mogilevtsev, Z. Hradil, and J. Peřina, "Homodyne reconstruction of density matrix in fock-state basis: Deterministic versus maximum likelihood approach", J. Mod. Opt. **44**, 2261–2269 (1997).

[148] I. Bengtsson and K. Zyczkowski, *Geometry of Quantum States: An Introduction to Quantum Entanglement* (Cambridge University Press, Cambridge, England, UK, 2006).

[149] S. Diamond and S. Boyd, "CVXPY: A Python-Embedded Modeling Language for Convex Optimization", Journal of machine learning research : JMLR **17**, 83 (2016).

[150] A. Agrawal, R. Verschueren, S. Diamond, and S. Boyd, "A rewriting system for convex optimization problems", Journal of Control and Decision **5**, 42–60 (2018).

[151] "CVXPY website", [Online; accessed 9. Jul. 2021] (2021).

[152] C. Eichler, D. Bozyigit, C. Lang, L. Steffen, J. Fink, and A. Wallraff, "Experimental State Tomography of Itinerant Single Microwave Photons", Phys. Rev. Lett. **106**, 220503 (2011).

[153] O. Hahn, P. Holmvall, P. Stadler, G. Ferrini, and A. Ferraro, "Deterministic Gaussian conversion protocols for non-Gaussian single-mode resources", Phys. Rev. A **105**, 062446 (2022).

[154] Intermodulation Products AB, "On digital synthesis and detection of microwave signals for quantum technology", [Online; accessed 17. Aug. 2022] (2021).

[155] J. Nokkala, R. Martínez-Peña, G. L. Giorgi, V. Parigi, M. C. Soriano, and R. Zambrini, "Gaussian states of continuous-variable quantum systems provide universal and versatile reservoir computing - Communications Physics", Commun. Phys. **4**, 1–11 (2021).

[156] J. Biamonte, P. Wittek, N. Pancotti, P. Rebentrost, N. Wiebe, and S. Lloyd, "Quantum machine learning", Nature **549**, 195–202 (2017).